

An Equilibrium Statistical Theory for Large-Scale Features of Open-Ocean Convection

MARK T. DiBATTISTA AND ANDREW J. MAJDA

Courant Institute of Mathematical Sciences, New York University, New York, New York

(Manuscript received 28 October 1998, in final form 28 July 1999)

ABSTRACT

A “most probable state” equilibrium statistical theory for random distributions of hetons in a closed basin is developed here in the context of two-layer quasigeostrophic models for the spreading phase of open-ocean convection. The theory depends only on bulk conserved quantities such as energy, circulation, and the range of values of potential vorticity in each layer. For a small Rossby deformation radius typical for open-ocean convection sites, the most probable states that arise from this theory strongly resemble the saturated baroclinic states of the spreading phase of convection, with a rim current and localized temperature anomaly. Furthermore, rigorous explicit nonlinear stability analysis guarantees the stability of these steady states for a suitable range of parameters. Both random heton distributions in a basin with quiescent flow as well as heton addition to an ambient barotropic flow in the basin are studied here. Also, systematic results are presented on the influence of the Rossby deformation radius compared to the basin scale on the structure of the predictions of the statistical theory.

1. Introduction

Open-ocean deep convection, which occurs in the Labrador Sea, the Greenland Sea, and the Mediterranean Sea in the current world climate, is an important phenomenon that strongly influences the thermohaline circulation governing the poleward transport of heat in the ocean. These basins with open-ocean convection are characterized by a small Rossby deformation radius compared with the basin scale so that rotational effects become important on comparatively small length scales. For a recent comprehensive survey, see the review by Marshall and Schott (1999).

One important aspect of this phenomenon is the spread of heat and vorticity through the ocean interior in response to a strong surface cooling event. It is obviously an interesting problem to develop simplified statistical theories that predict the extent and structure of the spreading phase of open-ocean convection relying only on bulk conserved quantities such as energy and circulation without resolving the fine-structure details of the dynamics. Such theories potentially can yield effective parameterization of the mesoscale effects of open-ocean convection in ocean general circulation models.

In this paper we develop such an equilibrium statis-

tical theory and analyze its predictions in the context of heton models that have been utilized in the two-layer quasigeostrophic equations to predict the spreading phase of open-ocean convection (Legg and Marshall 1993; Legg et al. 1996; Legg and Marshall 1998). In these models, random distributions of elementary hetons (Hogg and Stommel 1985) model the geostrophically balanced response to the convective mixing that results from localized surface cooling. This convective mixing yields a localized exchange of mass between the warmer upper layer and colder lower layer and is modeled in the two-layer quasigeostrophic equations through a heton as a local temperature anomaly, which raises the interface between the colder water below and the warmer water above.

In Legg and Marshall (1993) and Legg et al. (1996) the heton model is used to investigate the short-term generation and maintenance of a “convection chimney” produced by surface cooling within a localized domain. These studies find that, within a few days, a rough balance is established in the cooling region between buoyancy lost at the surface and buoyancy gained internally through the lateral propagation of heton clouds outside the region of localized forcing. These ejected heton clouds are composed of positive and negative point-vortex clusters whose centers are horizontally displaced (so that the energy contains a barotropic component) and whose strengths are generally unequal (so that the clouds tend to rotate about the forcing region). At relatively short times this convective chimney possesses a stable, cold baroclinic core, which is a kind of large

Corresponding author address: Dr. Andrew J. Majda, Courant Institute of Mathematical Sciences, New York University, 251 Mercer St., New York, NY 10012-1185.
E-mail: jonjon@cims.nyu.edu

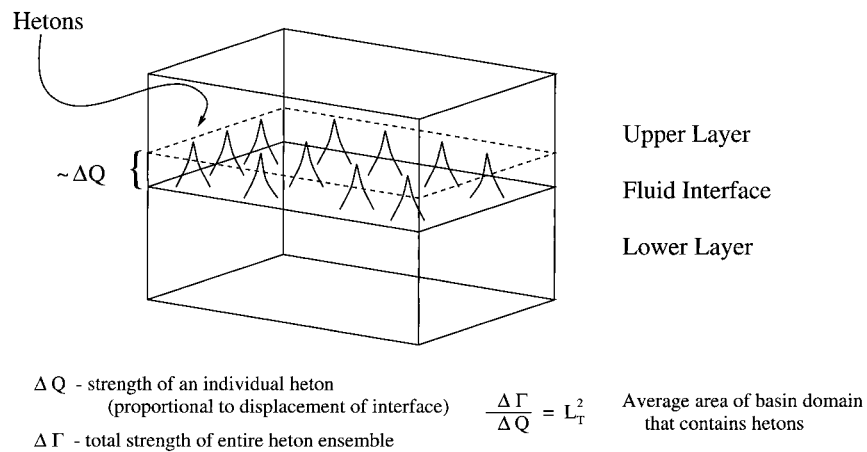


FIG. 1. Schematic showing the distribution of hetons in the initial ensemble. The heton strength parameter, ΔQ , is proportional to the displacement of the interface in a two-layer quasigeostrophic model. The length parameter, $L_T^2 = \Delta Q / \Delta \Gamma$, measures the average area of the unit basin that is initially seeded with hetons.

heton surrounded by propagating clouds of ejected heton pairs that collectively establish a stabilizing barotropic rim current.

In the present paper the heton model is used to parameterize statistically the small-scale vorticity field, which enters the equilibrium statistical theory as a prior probability distribution, resulting from a homogeneous, basinwide cooling event. Here, hetons effectively model the convective mixing, which produces convective chimneys, on the order of a deformation radius. The statistical theories developed here attempt to predict the longer-term lateral mixing of such a statistical ensemble of local convection events over the entire basin. The most-probable structures at statistical equilibrium share some large-scale features with the dynamical heton studies of Legg and Marshall (1993) and Legg et al. (1996)—here, the homogeneously distributed hetons congregate to form a baroclinic cold anomaly, which is a kind of giant heton, within a localized region in the center of the basin, governed by a stabilizing barotropic rim current.

The heton studies of Legg and Marshall (1993) and Legg et al. (1996) and the current equilibrium statistical model apply to physical phenomena established on very different spatial and temporal scales. The heton studies apply to convective chimneys, which are established within a few days over length scales of a few deformation radii. The present study furnishes predictions over the basin scale at times sufficiently large to allow the complete lateral mixing of many convective chimneys produced by a basinwide surface cooling event. We find it intriguing, however, that there are qualitative similarities in the results of these two types of investigation.

This paper is organized as follows. After a preliminary background discussion on the two-layer quasigeostrophic equations in section 2, we introduce the heton

model for convective mixing in section 3. This model uses elementary point-vortex structures called hetons (Hogg and Stommel 1985) for the localized geostrophically balanced response to surface cooling (Legg and Marshall 1993). The heton model is defined by two parameters: ΔQ , which is the strength of the elementary hetons; and $\Delta \Gamma$, which is the total circulation of the heton anomaly of the cooling event nondimensionalized by the basin scale (see, e.g., Fig. 1). By incorporating these two parameters, which contain the physical information of the basinwide cooling event, into least-biased probability measures for the two-layer potential vorticities, we develop an important link between the heton models and equilibrium statistical theories described in section 4.

The “most probable state” equilibrium statistical theory involves a “maximum entropy” principle that utilizes only a few physical constraints involving the total energy, the total circulation in each layer, and the a priori extrema of potential vorticity in each layer. The statistical theory yields specific equilibrium solutions of the inviscid two-layer quasigeostrophic equations that represent the most probable mean-field large-time response to a statistical ensemble of hetons generated by a surface cooling event consistent with the above constraints. There is both rigorous mathematical (DiBattista et al. 1998; Turkington 1999) and computational evidence in more idealized settings (Majda and Holen 1997; Grote and Majda 1997; DiBattista and Majda 1999, manuscript submitted to *Physica D*) for the validity and utility of the predictions of such a statistical theory employing these constraints. Conditions guaranteeing the nonlinear (and linearized) stability of the mean-field statistical steady states are developed in section 4 and applied throughout the paper.

The predictions of the equilibrium statistical theory for the spreading phase are presented in sections 5 and

6 for a wide parameter range of the bulk conserved quantities. In section 5 these results are presented for statistical heton distributions in a quiescent rectangular basin. The controlling parameter in a two-layer quasigeostrophic model is the “rotational Froude number,” F , defined by $F = (L/L_\rho)^2$ with L the length scale for the basin and L_ρ the Rossby deformation radius. For the situation with a small Rossby deformation radius compared to the basin scale ($F = 400$), the typical most probable states are localized monopoles with asymmetric concentrations of vorticity in the two layers, which we call “asymmetric monopoles,” with the overwhelming energy contribution being barotropic and the temperature anomaly confined within the region of strong barotropic flow. Thus, for homogeneous basin-wide buoyancy forcing the statistical theory automatically predicts a confined temperature anomaly within a stabilizing rim current, which is structurally similar to the numerical integration of heton models (Legg and Marshall 1993; Legg et al. 1996), that are valid on the chimney scale.

The nonlinear stability or baroclinic instability of the predicted equilibrium statistical structure for fixed energy depends crucially on the nondimensional parameter,

$$L_T^2 = \frac{\Delta\Gamma}{\Delta Q}, \tag{1.1}$$

where ΔQ is the maximum amplitude of potential vorticity anomaly over a deformation radius and $\Delta\Gamma$ is the total circulation generated by the cooling event, which is nondimensionalized by the basin scale (see, e.g., Fig. 1). Low values of L_T describe patchy initial heton baths, where buoyancy forcing is scattered across the basin. Higher values of L_T describe a more uniform buoyancy loss. As L_T increases, the saturated equilibrium state becomes proveably nonlinearly stable at fixed energy while the temperature anomaly spreads to larger scales. We end section 5 with a discussion of the effect of a larger Rossby radius on the predictions of the statistical theory. For example, for a large deformation radius ($F = 4$), most of the energy is baroclinic and the temperature anomaly is spread throughout the domain on a larger scale than the barotropic flow. In section 6, we study the important physical situation when a statistical ensemble of hetons in a cooling event is added to a preexisting ambient barotropic flow in the basin (Legg and Marshall 1998, and references therein). Both strong and weak preexisting barotropic flows are considered there.

2. Two-layer quasigeostrophic formalism

In this paper we study the large-scale vortex structures that emerge as the most probable states of an equilibrium statistical theory following a basinwide cooling event. We apply this theory, which involves only a few constraints such as energy, circulation, and potential vor-

ticity extrema, to the simplest fluid model with a nontrivial vertical structure, the two-layer quasigeostrophic model.

a. Two-layer quasigeostrophic fluid model

Specifically, our stably stratified, two-layer quasigeostrophic fluid evolves in a unit basin, with extent $-\frac{1}{2} < x < \frac{1}{2}$ and $-\frac{1}{2} < y < \frac{1}{2}$. Within each layer the fluid is assumed to have constant density, ρ_1 and ρ_2 , and identical depth, $D/2$, so that F , the “rotational Froude number,” is the same for both layers (Pedlosky 1979). In the two-layer model the reduced gravity, $g' = (\rho_1 - \rho_2)/\rho_0$, where ρ_0 is a reference density, is equivalent to the buoyancy anomaly experienced by a displaced fluid parcel. The potential vorticities of the upper and lower layers, q_1 and q_2 , and the upper- and lower-layer streamfunctions, ψ_1 and ψ_2 , are coupled through the relations,

$$\begin{aligned} q_1 &= \Delta\psi_1 - F(\psi_1 - \psi_2) \\ q_2 &= \Delta\psi_2 + F(\psi_1 - \psi_2). \end{aligned} \tag{2.1}$$

Here, the symbol $\Delta \equiv \partial^2/\partial x^2 + \partial^2/\partial y^2$ is the Laplacian operator in two dimensions and the nondimensional parameter F is the square of the ratio of length scales, $F = 1/L_\rho^2$, where L_ρ is Rossby deformation radius nondimensionalized by the (unit) basin length scale. The dynamic equation for the two-layer fluid is expressed by the material conservation of potential vorticity in each layer,

$$\begin{aligned} \frac{\partial q_1}{\partial t} + \nabla^\perp \psi_1 \cdot \nabla q_1 &= 0 \\ \frac{\partial q_2}{\partial t} + \nabla^\perp \psi_2 \cdot \nabla q_2 &= 0, \end{aligned} \tag{2.2}$$

where the symbol $\nabla^\perp \equiv \mathbf{k} \times \nabla$ is the perpendicular gradient operator. Together with the conditions of no normal flow at the lateral boundaries of the basin,

$$\begin{aligned} \frac{\partial \psi}{\partial x} &= 0, & y &= \pm 1/2, \\ \frac{\partial \psi}{\partial y} &= 0, & x &= \pm 1/2, \end{aligned} \tag{2.3}$$

the evolution of the two-layer fluid is completely determined by the initial potential vorticities.

It is well known that the system of equations in (2.2) and (2.3) conserves the energy

$$E = -\sum_{j=1}^2 \int q_j \psi_j \, dA, \tag{2.4}$$

the circulations in each layer

$$\Gamma_j = \int q_j \, dA, \quad j = 1, 2, \tag{2.5}$$

and, indeed, any arbitrary function \mathcal{G} of the potential vorticity in each layer

$$\int \mathcal{G}(q_j) dA, \quad j = 1, 2. \quad (2.6)$$

This last family of conserved quantities in (2.6) is a consequence of the material conservation of potential vorticity in each layer.

b. Energy components

The energy in a two-layer model, with nonzero F , has three distinct components: the kinetic energy divided into barotropic and baroclinic portions and the potential energy determined by the baroclinic component of the streamfunction. It is easy to show that, given the following definition of barotropic and baroclinic components, ψ_B and ψ_T ,

$$\psi_B = \frac{\psi_1 + \psi_2}{\sqrt{2}} \quad \psi_T = \frac{\psi_1 - \psi_2}{\sqrt{2}}, \quad (2.7)$$

the total energy, E , is conserved,

$$E = E_B + K_T + P, \quad (2.8)$$

where the energy components are defined by

$$\begin{aligned} \text{Barotropic:} \quad E_B &= \frac{1}{2} \int |\nabla \psi_B|^2 \\ \text{Baroclinic kinetic:} \quad K_T &= \frac{1}{2} \int |\nabla \psi_T|^2 \\ \text{Potential:} \quad P &= F \int \psi_T^2. \end{aligned} \quad (2.9)$$

The relation in (2.8) is easily demonstrated since

$$\begin{aligned} E &= -\frac{1}{2} \int (\psi_1 q_1 + \psi_2 q_2) \\ &= \frac{1}{2} \int (|\nabla \psi_1|^2 + |\nabla \psi_2|^2) + \frac{F}{2} \int (\psi_1 - \psi_2)^2. \end{aligned} \quad (2.10)$$

Furthermore, substitution of the barotropic and baroclinic components in (2.7) yields

$$E = \frac{1}{2} \int (|\nabla \psi_B|^2 + |\nabla \psi_T|^2) + F \int \psi_T^2, \quad (2.11)$$

which satisfies the claim.

c. Temperature anomaly

The deformation of the interface between the upper and lower layers of the quasigeostrophic fluid is proportional to the baroclinic streamfunction, ψ_T (Pedlosky 1979):

$$h = \frac{D}{2} - \epsilon F \psi_T, \quad (2.12)$$

where h is the height of the perturbed interface, and ϵ

is Rossby number, which is small. Since the fluid is of constant density within each layer, this quantity is directly proportional to the temperature anomaly, which we therefore define as

$$-F \psi_T. \quad (2.13)$$

A perturbation that pushes the fluid interface upward and establishes a local maximum is associated with a cyclonic vortex in the upper layer and a matching anticyclonic vortex in the lower layer. Since this is the general effect of convective overturning in the fluid, we call this a positive anomaly because the interface between the warmer water in the upper layer and the colder water in the lower layer has been raised.

3. The link between equilibrium statistical theories and heton models for open-ocean convection

Heton models have been used in the context of the two-layer quasigeostrophic equations as simplified models for predicting the lateral spread of heat and vorticity resulting from localized surface buoyancy forcing over several deformation radii (Legg and Marshall 1993; Legg et al. 1996; Legg and Marshall 1998). Here, the heton model is used to parameterize the small-scale vorticity field resulting from a basinwide cooling event. The heton model is parameterized by two physical parameters: ΔQ , which is the maximum strength of the potential vorticity anomaly over a deformation length due to buoyancy forcing, and $\Delta \Gamma$, which gives the total circulation anomaly associated with an ensemble of hetons distributed throughout the domain. Least-biased probability measures for the potential vorticity based on these parameters, which contain the physical information associated with a basinwide cooling event, establish an important link between heton models and the equilibrium statistical theories that follow in section 4. First, we discuss the case of purely baroclinic heton forcing in a quiescent ocean basin in detail as the simplest case and then we describe the more general situation for utilizing the statistical theory with preexisting barotropic and baroclinic flow structure.

a. Heton model parameters

An elementary heton (Hogg and Stommel 1985) is a purely baroclinic point-vortex structure with potential vorticity of the form

$$q_1(\mathbf{x}) = \Delta q_j \delta_{\mathbf{x}_j}, \quad q_2(\mathbf{x}) = (-\Delta q_j) \delta_{\mathbf{x}_j} \quad (3.1)$$

where $\Delta q_j > 0$ is the strength of the heton, $\mathbf{x}_j = (x_j, y_j)$ is a random location in the basin, and $\delta_{\mathbf{x}}$ is the Dirac delta function at \mathbf{x} . Such elementary hetons are introduced by Legg and Marshall (1993) to model the geostrophically balanced response to the small-scale convective mixing that results from local surface cooling. This convective mixing yields a localized exchange of mass between the warmer upper layer and colder lower

layer and is modeled in the two-layer quasigeostrophic equations via (3.1) as a local thermal anomaly [see (2.13)], which raises the interface between the colder water below and the warmer water above.

For small Rossby deformation radius, $L_\rho \ll 1$, typical in regions of open-ocean convection, the local thermal anomaly and flow field are strongly confined within the distance $O(L_\rho)$ to the vicinity of the location \mathbf{x}_j . For the heton pair in (3.1), the potential vorticity structure is purely baroclinic, and the upper-layer flow is cyclonic while the lower-layer flow is anticyclonic. The effect of surface cooling over a finite region is modeled by a superposition of the heton structures in (3.1) with random locations \mathbf{x}_j confined within the cooling regions and separated by L_ρ with a constant potential vorticity anomaly, $\Delta q_j = \Delta Q$, independent of j . The total strength of the basinwide cooling event, determined by total strength of the hetons, is given by the total circulation anomaly,

$$\int q_1 = - \int q_2 = \Delta \Gamma. \tag{3.2}$$

The parameter $\Delta \Gamma$ depends on the total buoyancy lost over the cooling period, which may vary both temporally and spatially. We stress that the relation in (3.2) between the heton forcing strength and total circulation requires that hetons be spaced by at least a deformation radius, which ensures that the total circulation is finite in the unit basin. For the detailed analytical formulas associated with the above heton model, we refer the reader to Legg and Marshall (1993) or Marshall and Schott (1999).

The parameters ΔQ and $\Delta \Gamma$, which describe the maximum and total potential vorticity in the ocean interior, carry the physical information in the heton model associated with the basinwide cooling event. This can be shown by expressing these parameters explicitly in terms of the surface buoyancy flux, $B_0(\mathbf{x})$, which is directly related to the surface heat loss that controls open-ocean convection (Marshall and Schott 1999). At length and timescales comparable to the earth's rotation, $1/f$, and to the deformation radius, L_ρ , respectively, the towers formed by convective mixing are in approximate thermal wind balance, so

$$\Delta Q \sim \frac{g' \eta}{f L_\rho^2}, \tag{3.3}$$

where ΔQ is the local potential vorticity anomaly over a deformation radius, g' is the reduced gravity in the two-layer model, and η is the average displacement of the fluid interface. In the two-layer model the buoyancy flux, B_0 , lost at the surface is balanced by a conversion of upper-layer fluid to lower-layer fluid at the interior interface, whose buoyancy per unit volume therefore changes by the reduced gravity, g' . Within the timescale, $1/f$, and the length scale, L_ρ , this balance of total surface flux and interior buoyancy loss is approximated by

$$fg' \eta \sim B_0. \tag{3.4}$$

Combining the thermal wind relation in (3.3) and detailed balance of buoyancy in (3.4) yields the strength of the potential vorticity anomaly, ΔQ , in terms of a prescribed surface buoyancy forcing, B_0 ,

$$\Delta Q \sim \frac{B_0}{f^2 L_\rho^2}. \tag{3.5}$$

The parameter, ΔQ , which is the strength of an individual heton expressed over a deformation radius, measures the local effect of surface cooling. The parameter, $\Delta \Gamma$, however, is a measure of the total number of hetons—each spaced by at least a deformation radius—introduced into the basin, which is determined by the spatial variability of the buoyancy flux, $B_0(\mathbf{x})$. Thus, it is possible to develop a more complicated program in terms of the surface buoyancy flux, B_0 , by dividing the basin domain into a grid with spacing L_ρ in which a heton is added to the box centered at \mathbf{x} in whose strength is determined by the local buoyancy flux, $B_0(\mathbf{x})$ in (3.5). Note that the parameter, $\Delta \Gamma$, reaches a maximum for a uniform cold air outbreak across the entire basin. Here the heton strength, ΔQ , and the maximum total circulation, $\Delta \Gamma_{\max}$, are related by

$$\Delta \Gamma_{\max} = A \Delta Q, \tag{3.6}$$

where A is the area of the basin. Armed with the relation in (3.6), however, we may dispense with specifying a particular surface buoyancy flux, $B_0(\mathbf{x})$, and completely define the physical effects of surface cooling with the parameters ΔQ and $\Delta \Gamma$, taking care that $\Delta \Gamma \leq A \Delta Q$. Indeed, one advantage to this approach is that we reduce the whole assortment of possible surface buoyancy flux functions $B_0(\mathbf{x})$ into equivalence classes defined by ΔQ and $\Delta \Gamma$, which are quantities easily absorbed into the statistical theory. Furthermore, it is a simple matter to extend the above model to account for temporal and spatial variability in the cold air outbreaks, a detail that does not change the interpretation of the key parameters.

An important parameter measuring the statistical spreading of hetons is given by

$$L_T = \sqrt{\frac{\Delta \Gamma}{\Delta Q}}. \tag{3.7}$$

We note that the nondimensional parameter L_T roughly measures the square root of the area of heton spreading divided by the basin area with $0 \leq L_T \leq 1$ (see, e.g., Fig. 1). The value of L_T naturally depends on the variability of the surface buoyancy flux, $B_0(x)$. At low values of L_T the buoyancy forcing is patchy and scattered across the basin. At high values of L_T the buoyancy forcing is spread more evenly across the basin—a uniform cold air outbreak over the entire basin leads to the maximum condition, $L_T = 1$. Thus, for fixed energy, small deformation radius, and in a quiescent background, we establish below in section 5b that the pa-

parameter L_T controls the extent of significant thermal anomaly in the most probable coarse-grained statistical state.

b. Heton models and the equilibrium statistical theory

The heton model parameters, ΔQ and $\Delta\Gamma$, give the peak potential vorticity and total circulation in a two-layer model following a surface cooling event. The link between the heton model and the equilibrium statistical theory is established by determining the least-biased distribution of potential vorticity throughout the basin consistent with these parameters. This least-biased distribution enters the equilibrium statistical theory, which is introduced in section 4, as a prior probability measure for the microscale potential vorticity.

For an ensemble of hetons seeded in a quiescent flow, where the only available prior information is the strength, ΔQ , the least-biased distributions, Π_{0j} , for the potential vorticity in the upper and lower layers are given by

$$\Pi_{01}(\lambda) = \frac{1}{\Delta Q} I_0^{\Delta Q}(\lambda) \quad \Pi_{02}(\lambda) = \frac{1}{\Delta Q} I_0^{-\Delta Q}(\lambda), \quad (3.8)$$

where I_0^a represents a uniform distribution over the interval $[a, b]$, and λ is the potential vorticity. The only initial physical information here is the maximum amplitude of the statistical ensemble of hetons, which may be determined by the buoyancy anomaly, B_0 . Note from (3.8) that there is no spatial dependence in the prior measures, Π_{0j} , so that the cooling event is assumed tacitly to occur over the entire basin (Legg et al. 1998) and not over a localized region.

If, in addition to the heton strength, ΔQ , we are also given the total circulation, $\Delta\Gamma$, introduced by the spatial and temporal variability of the buoyancy forcing, how do we find the least-biased prior probability distribution for a statistical ensemble of hetons? This follows from a standard information-theoretic procedure (Jaynes 1957) that we develop more fully in section 4. The results are the probability densities for the microscale distribution of hetons,

$$\begin{aligned} \Pi_{01}^*(\lambda) &= \frac{e^{-\gamma_1\lambda}\Pi_{01}(\lambda)}{\int e^{-\gamma_1\lambda}\Pi_{01}(\lambda) d\lambda} \\ \Pi_{02}^*(\lambda) &= \frac{e^{-\gamma_2\lambda}\Pi_{02}(\lambda)}{\int e^{-\gamma_2\lambda}\Pi_{02}(\lambda) d\lambda}. \end{aligned} \quad (3.9)$$

In (3.9) the two constants, γ_j (with $\gamma_2 = -\gamma_1$ for surface cooling over quiescent flow), are determined uniquely by the conditions

$$\int \lambda \Pi_{0j}^*(\lambda) d\lambda = (-1)^{j+1} \frac{\Delta\Gamma}{A}, \quad (3.10)$$

where A is the area of the basin.

We can interpret the prior probability measures in (3.9) in the following manner: pick the locations, \mathbf{x}_j , at random in the basin and pick the heton strengths, Δq_j , at random from the probability distributions, $\Pi_{0j}^*(\lambda)$; then the law of large numbers (Lamperti 1966) guarantees that the probability measures, $\Pi_{01}^*(\lambda)$ and $\Pi_{02}^*(\lambda)$, given uniformly over the basin are well approximated by superpositions of random heton structures,

$$q_1 = \frac{1}{N} \sum_{j=1}^N \Delta q_j \delta_{\mathbf{x}_j} \quad q_2 = \frac{1}{N} \sum_{j=1}^N (-\Delta q_j) \delta_{\mathbf{x}_j}, \quad (3.11)$$

for large enough values of N . Thus, with (3.11) we interpret the most probable state statistical theory described in section 4 as computing the most likely coarse-grained macrostate that emerges from a cooling event over the entire basin that generates a random distribution of local mixing events as hetons consistent with the amplitude ΔQ , the circulation $\Delta\Gamma$, and some prescribed energy. A schematic of the initial heton ensemble is shown in Fig. 1.

How do we reconcile the definitions for heton baths provided by (3.1) and (3.11)? In some sense we have generalized the heton definitions introduced in Legg and Marshall (1993) to account for mixing processes that occur on spatial scales below the deformation radius. Thus, the singularities that appear in (3.1), which are spaced by at least a deformation radius, are in some sense further divided in (3.11) into an arbitrarily large number of singularities whose individual strengths are vanishingly small but contribute a strength of, at most, ΔQ when smoothed over a deformation scale.

c. Prior distributions for general flow fields

In this section we calculate the prior probability measures consistent with a cooling event over the basin with a preexisting ambient barotropic flow. The heton model parameters, ΔQ and $\Delta\Gamma$, determined by the surface cooling event, naturally do not change; however, we provide two more parameters, Q_B and Γ_B , which measure the peak vorticity and the total circulation in the ambient large-scale barotropic flow, and modify the prior measures, Π_{0j} in (3.8), and Π_{0j}^* in (3.9), to account for the additional information.

For a purely barotropic flow the potential vorticity is symmetric with respect to the upper and lower layers. Thus, the potential vorticity maximum, Q_B , is identical in both layers. In the simplest case the potential vorticity for cyclonic flow is entirely positive so that the microstructure potential vorticity in both layers is given by the prior probability measure

$$\Pi_B(\lambda) = \frac{1}{Q_B} I_0^{Q_B}(\lambda), \quad j = 1, 2, \quad (3.12)$$

where I_0^a represents a uniform distribution over the interval $[a, b]$. For barotropic flow the large-scale circulations in both layers are also equal so that

$$\int q_1 = \int q_2 = \Gamma_B, \tag{3.13}$$

where q_1 and q_2 are the potential vorticities in the upper and lower layers.

Now, for a general random mixture of hetons with the prior distribution in (3.8)—corresponding to cold anomalies—and a barotropic flow with the prior distribution in (3.12), the maximum potential vorticity in the upper layer is increased, while the minimum potential vorticity in the lower layer is decrease, yielding

upper-level extrema:

$$q_{1,\max} = Q_B + \Delta Q, \quad q_{1,\min} = 0$$

lower-level extrema:

$$q_{2,\max} = Q_B, \quad q_{2,\min} = -\Delta Q. \tag{3.14}$$

The circulations in the upper and lower layers are modified by the cold air outbreak and are given by

$$\int q_1 = \Gamma_B + \Delta\Gamma \quad \int q_2 = \Gamma_B - \Delta\Gamma. \tag{3.15}$$

How then do we express the prior information on the upper- and lower-level potential vorticities given the potential vorticity extrema in (3.14) and the circulations in (3.15)? We simply repeat the calculations introduced in section 3b so that the prior probability distributions, Π_{0j}^* , take the form

$$\begin{aligned} \Pi_{01}^*(\lambda) &= \frac{e^{-\gamma_1\lambda}\Pi_{01}(\lambda)}{\int e^{-\gamma_1\lambda}\Pi_{01}(\lambda) d\lambda} \\ \Pi_{02}^*(\lambda) &= \frac{e^{-\gamma_2\lambda}\Pi_{02}(\lambda)}{\int e^{-\gamma_2\lambda}\Pi_{02}(\lambda) d\lambda}, \end{aligned} \tag{3.16}$$

where the probability measures, Π_{0j} , for the vorticity extrema given in (3.14) are

$$\begin{aligned} \Pi_{01}(\lambda) &= \frac{1}{Q_B + \Delta Q} I_{0}^{Q_B + \Delta Q} \\ \Pi_{02}(\lambda) &= \frac{1}{Q_B + \Delta Q} I_{0}^{Q_B - \Delta Q}, \end{aligned} \tag{3.17}$$

and the Lagrange multipliers, γ_j , must satisfy

$$\begin{aligned} \int \lambda \Pi_{01}^*(\lambda) d\lambda &= \frac{\Gamma_B + \Delta\Gamma}{A} \\ \int \lambda \Pi_{02}^*(\lambda) d\lambda &= \frac{\Gamma_B - \Delta\Gamma}{A}, \end{aligned} \tag{3.18}$$

where A is the area of the basin. The prior measure, Π_{0j}^* in (3.16), therefore yields the microscale distribution of potential vorticity with least-bias given a preexisting barotropic flow with potential vorticity maximum, Q_B ,

and circulation, Γ_B , in each layer, and a basin wide cooling event defined by the heton strength parameter, ΔQ , and total circulation anomaly, $\Delta\Gamma$.

d. Basin geometry and nondimensionalization

In the subsequent sections we compute the most probable statistical states that emerge in a rectangular basin geometry. We nondimensionalize length scales by the length of the side of the basin and we nondimensionalize potential vorticity for both layers by the interval width of the prior distribution, $Q_B + \Delta Q$. Thus, all results presented below assume a unit rectangular basin geometry with a unit interval width for the potential vorticity in the prior distributions for each layer. Since $Q_B + \Delta Q$ has units of (time)⁻¹, all other physical quantities are nondimensionalized in terms of these time and length scales.

4. The Langevin equilibrium statistical theory

In sections 3b and 3c we calculated the prior probability measures, Π_{0j}^* in (3.9) and (3.16), that capture the physical information contained in a basinwide surface cooling event over quiescent and preexisting barotropic flow, respectively. In this section we develop an equilibrium statistical theory for the spreading phase of open-ocean convection that contains the least bias given only the large-scale energy, E in (2.4), and these distributions, Π_{0j}^* , that contain the prior information on the microscale vorticity field. This theory, which is tailored for the two-layer quasigeostrophic model discussed in section 2, yields the long-term distributions of heat and potential vorticity introduced by the flux of buoyancy from the ocean surface due to a cold air outbreak.

The prior distributions, Π_{0j}^* , encode the microscale potential vorticity based on only *two* of the infinite vortical invariants for two-layer quasigeostrophic flow listed in (2.6), namely, the potential vorticity extrema and the circulations in each layer. Strong support for basing an equilibrium statistical theory on a few robust constraints, rather than the full infinite list, has been given in numerical and theoretical investigations into damped and driven flow in a single layer (Majda and Holen 1997; Grote and Majda 1997). Indeed, recent studies using only the constraints on the energy, the circulation, and the potential vorticity extrema, which yields an equilibrium statistical theory known as the Langevin statistical theory (Turkington 1999), have calculated the statistically most probable mean-field states for single-layer quasigeostrophic flow in a β -plane channel (DiBattista et al. 1998) and have demonstrated the metastability of these flows to strong damping and driving (DiBattista and Majda 1999, manuscript submitted to *Physica D*). Furthermore, the Langevin equilibrium statistical theory correctly follows the topological structure of these damped and driven flows even as vortex struc-

tures cross into zonal shears and vice versa (DiBattista and Majda 1999, manuscript submitted to *Physica D*).

In general, a statistical mechanics theory for fluid flow maximizes the information (Jaynes 1957), expressed in terms of entropy, contained in the finescale vorticity field to yield the most probable coarse-grained field. The finescale field is represented as a prior distribution; the coarse-grained field is represented by the one-point probability distributions, $\rho_1(\mathbf{x}, \lambda)$ and $\rho_2(\mathbf{x}, \lambda)$, one for each layer, where the parameter λ varies over the range of potential vorticities allowed by the prior distribution. Thus, for any point \mathbf{x} in the basin domain the probability distribution for potential vorticity in each layer within the potential vorticity range, α_j to β_j , is described by $\rho_j(\mathbf{x}, \lambda)$:

$$\text{prob}\{\alpha_j \leq q_j(\mathbf{x}) \leq \beta_j\} = \int_{\alpha_j}^{\beta_j} \rho_j(\mathbf{x}, \lambda) d\lambda, \quad j = 1, 2. \quad (4.1)$$

As the fluid evolves into ever finer scales, the dominant coarse-grained potential vorticities, \bar{q}_1 and \bar{q}_2 , emerge on the largest scale—the solutions observed at long times. In the statistical theory, the one-point distributions and the mean-field quantities are related by the mean-field equations,

$$\bar{q}_1 = \int \lambda \rho_1(\mathbf{x}, \lambda) d\lambda \quad \bar{q}_2 = \int \lambda \rho_2(\mathbf{x}, \lambda) d\lambda, \quad (4.2)$$

which together with the vorticity–streamfunction relations, (2.1), and the boundary conditions, (2.3), give a coupled, nonlinear elliptic equation for the mean-field streamfunctions, $\bar{\psi}_1$ and $\bar{\psi}_2$.

For the heton ensemble that models open-ocean convection, the prior probability distributions, which encode the prior information in the finescale field, are given by the measures Π_{0j}^* in (3.9) for surface cooling over quiescent flow or (3.16) for cooling over ambient barotropic flow. The coarse-grained one-point probability distributions, ρ_1 and ρ_2 , that contain the least bias maximize the Shannon entropy, S , subject to the prior distributions in each layer, $\Pi_{01}^*(\lambda)$ and $\Pi_{02}^*(\lambda)$ (Jaynes 1957),

$$S(\rho_1, \rho_2, \Pi_{01}^*, \Pi_{02}^*) \equiv - \sum_{j=1}^2 \iint \rho_j(\mathbf{x}, \lambda) \ln \frac{\rho_j(\mathbf{x}, \lambda)}{\Pi_{0j}^*(\lambda)} d\lambda dA. \quad (4.3)$$

The distributions ρ_1 and ρ_2 are constrained by the energy, in (2.4), and probability definition, in (4.1), which are expressed as the family of constraints $C = C^{(1)} \cap C^{(2)} \cap C^{(3)}$,

$$C^{(1)} = \left\{ (\rho_1, \rho_2) \mid E(\rho_1, \rho_2) = - \int \frac{1}{2} \bar{\psi}_1 \bar{q}_1 dA - \int \frac{1}{2} \bar{\psi}_2 \bar{q}_2 dA = E \right\}, \quad (4.4)$$

$$C^{(2)} = \left\{ \rho_1 \mid M(\rho_1) = \int \rho_1(\mathbf{x}, \lambda) d\lambda = 1, \text{ for each } \mathbf{x} \right\},$$

$$C^{(3)} = \left\{ \rho_2 \mid M(\rho_2) = \int \rho_2(\mathbf{x}, \lambda) d\lambda = 1, \text{ for each } \mathbf{x} \right\}.$$

Thus, the probability distributions ρ_1 and ρ_2 must satisfy all three conditions in (4.4). Here the constraint in $C^{(1)}$ determines the energy in the large-scale flow, which includes both potential and kinetic energy components of the two-layer fluid. We recall that the energy is computed from ρ_1 and ρ_2 via the *mean* potential vorticities defined in (4.2). The constraints in $C^{(2)}$ and $C^{(3)}$ ensure that $\rho_1(\mathbf{x}, \lambda)$ and $\rho_2(\mathbf{x}, \lambda)$ satisfy the basic condition in (4.1) for a probability distribution at each point in the basin. Notice that the energy constraint is expressed in terms of the mean-field potential vorticity.

The maximization of (4.3) subject to the constraints (4.4) is generally solved by the method of Lagrange multipliers in the calculus of variations. We introduce the multipliers θ , and $\tilde{\mu}_j(\mathbf{x})$, which are associated with the energy and one-point probability constraints, respectively, in (4.4), where $j = 1, 2$ refer to the upper- and lower-level quantities. We extremize the functional

$$-S(\rho_1, \rho_2, \Pi_{01}^*, \Pi_{02}^*) + \theta(E(\rho_1, \rho_2) - E) + \sum_{j=1}^2 \tilde{\mu}_j(\mathbf{x})(M_j(\rho_j) - 1) \quad (4.5)$$

in which E is the imposed values of energy. By taking the first variation of (4.5) with respect to ρ_j ,

$$-\frac{\delta S}{\delta \rho_j} + \theta \frac{\delta E}{\delta \rho_j} + \tilde{\mu}_j \frac{\delta M_j}{\delta \rho_j} = 0,$$

substituting the functional derivatives

$$\frac{\delta S}{\delta \rho_j} = -1 - \ln \left(\frac{\rho_j}{\Pi_{0j}^*} \right), \quad \frac{\delta E}{\delta \rho_j} = -\bar{\psi}_j \lambda, \quad \frac{\delta M_j}{\delta \rho_j} = \delta_{\mathbf{x}} \otimes 1, \quad (4.6)$$

and enforcing the one-point probability constraints for each layer, $C^{(2)}$ and $C^{(3)}$, the functions $\rho_1(\mathbf{x}, \lambda)$ and $\rho_2(\mathbf{x}, \lambda)$ take the form

$$\rho_1(\mathbf{x}, \lambda) = \frac{e^{\theta \bar{\psi}_1 \lambda \Pi_{01}^*(\lambda)}}{\int e^{\theta \bar{\psi}_1 \lambda \Pi_{01}^*(\lambda)} d\lambda}, \quad \rho_2(\mathbf{x}, \lambda) = \frac{e^{\theta \bar{\psi}_2 \lambda \Pi_{02}^*(\lambda)}}{\int e^{\theta \bar{\psi}_2 \lambda \Pi_{02}^*(\lambda)} d\lambda}. \quad (4.7)$$

The most probable coarse-grained state is found by substituting the probability distribution in (4.7) into the mean-field potential vorticities in (4.2). Upon substi-

tution of the prior distributions for the heton ensemble, $\Pi_{\bar{\psi}_j}^*$ in (3.9), the mean-field equations for the spreading phase of open-ocean convection in ambient quiescent flow take the following form:

Mean-field equations for convective mixing in ambient quiescent flow

$$\begin{aligned} \bar{q}_1 &\equiv \Delta\bar{\psi}_1 - F(\bar{\psi}_1 - \bar{\psi}_2) \\ &= \frac{\Delta Q}{2} \left(1 + \mathcal{L} \left[\frac{\Delta Q}{2} (\theta\bar{\psi}_1 - \gamma_1) \right] \right) \\ \bar{q}_2 &\equiv \Delta\bar{\psi}_2 + F(\bar{\psi}_1 - \bar{\psi}_2) \\ &= -\frac{\Delta Q}{2} \left(1 - \mathcal{L} \left[\frac{\Delta Q}{2} (\theta\bar{\psi}_2 - \gamma_2) \right] \right), \end{aligned} \quad (4.8)$$

which, along with the boundary conditions in (2.3), are

a pair of coupled, nonlinear elliptic equations for the mean-field streamfunctions. Here, we have $\mathcal{L}[x] \equiv \coth[x] - 1/x$, which is known as the Langevin function. Note that the parameter ΔQ is the heton strength determined by the cooling event and the constants γ_j are determined through (3.10), which ensures that the circulations of the mean-field potential vorticities, \bar{q}_j , are given by the basinwide cooling event. Thus, the mean-field equations in (4.8) yield the mean-field potential vorticity fields expected to arise at statistical equilibrium following a basinwide cold-air outbreak over quiescent flow in a basin.

The mean-field equations for convective mixing in ambient barotropic flow, discussed in section 3c, are calculated by a similar procedure. Here, we substitute the prior distributions for the heton ensemble, $\Pi_{\bar{\psi}_j}^*$ in (3.16), and the mean-field equations for the spreading phase of open-ocean convection in ambient quiescent flow take the following form:

Mean-field equations for convective mixing in ambient barotropic flow

$$\begin{aligned} \bar{q}_1 &\equiv \Delta\bar{\psi}_1 - F(\bar{\psi}_1 - \bar{\psi}_2) \\ &= \frac{Q_B + \Delta Q}{2} + \frac{Q_B + \Delta Q}{2} \mathcal{L} \left[\frac{Q_B + \Delta Q}{2} (\theta\bar{\psi}_1 - \gamma_1) \right] \\ \bar{q}_2 &\equiv \Delta\bar{\psi}_2 + F(\bar{\psi}_1 - \bar{\psi}_2) \\ &= \frac{Q_B - \Delta Q}{2} + \frac{Q_B + \Delta Q}{2} \mathcal{L} \left[\frac{Q_B + \Delta Q}{2} (\theta\bar{\psi}_2 - \gamma_2) \right], \end{aligned} \quad (4.9)$$

which, along with the boundary conditions in (2.3), are a pair of coupled, nonlinear elliptic equations for the mean-field streamfunctions. The mean-field equations in (4.9) describe the most general case for a surface cooling event over a basin with a preexisting barotropic flow. The constants, γ_j , are determined by the relations in (3.18), which ensure that the most probable mean-field potential vorticities, \bar{q}_j , have the appropriate circulations.

To solve the Langevin mean-field equations, one must specify five large-scale conserved quantities: the energy E , the circulations associated with the cooling event $\Delta\Gamma$, the large-scale barotropic flow Γ_B , and the potential vorticity extrema, given the contributions from the heton forcing, ΔQ , and the preexisting ambient flow Q_B . The most probable states are calculated by an accurate iterative algorithm due to Turkington and Whitaker (1996) that simultaneously determines the mean-field streamfunctions, $\bar{\psi}_1$ and $\bar{\psi}_2$, and the Lagrange multipliers, θ , γ_1 , and γ_2 , that satisfy the given constraints. See DiBattista et al. (1998) for more details on the general algorithm.

a. Other statistical theories

We have based the preceding discussion on a new statistical theory (Turkington 1999) that is based on only a few conserved quantities, the energy, the vorticity extrema, and the total circulation. Naturally, one may construct theories from other vortical invariants. One such model is based on only two conserved quantities, the energy and enstrophy (Kraichnan 1975), and has been successfully employed in oceanographic settings, especially in flows dominated by topography (Salmon et al. 1976; Holloway 1986; Carnevale and Frederiksen 1987)—although there are alternative interpretations—and in flows with low energies and nearly minimal enstrophy that satisfy the conditions of selective decay (Bretherton and Haidvogel 1976). Why, then, have we chosen to forgo the nominally simpler energy–enstrophy theory, which uses fewer conserved quantities, in favor of the Langevin theory?

We have done so for two main reasons: First, the Langevin theory requires two parameters as we discussed in section 3—the potential vorticity extrema, ΔQ ,

and the total circulation anomaly, $\Delta\Gamma$ —that occur most naturally in parametrizing the heton ensemble. The potential vorticity extrema are directly related to the strength of the vortices that constitute the convective towers. The circulations induced in each layer are determined by the density of hetons seeded in the basin. Both of these quantities in turn are solely determined by the strength and distribution of the surface buoyancy flux, which drives convection in the ocean. Also, the Langevin theory is among the simplest theories that yield a nonlinear relation for the mean-field streamfunction that accounts for nearly all of the energy in the flow. The solutions from energy–enstrophy theory, in the absence of topography or β effect, have neither of these desirable properties. Finally, it is well known that the energy–enstrophy statistical theory predicts no mean flow without topography and a highly fluctuating vorticity structure with no mean energy in the continuum limit (Kraichnan 1975).

A second school of thought holds that equilibrium statistical theories must account for all vortical invariants conserved by ideal flow and attempt to preserve exactly the rearrangements of the initial vorticity field (Robert 1991; Miller et al. 1992). These recent theories, which are fully nonlinear, therefore require an infinite amount of information about the state of the flow. For a strongly damped and driven fluid, such as the ocean, the higher-order moments of the vorticity field may fluctuate rapidly in time, some lost to small scales in the enstrophy cascade, and some dissipated by viscosity. However, nearly all of these higher-order moments require more information about the instantaneous state of the ocean than is practically possible either to collect or to estimate accurately. Such theories have been used recently as a basis for parameterizing closure (Kazansev et al. 1998).

Thus, in some sense the energy–enstrophy theory is too simple for our purposes and the infinite-constraint theories too complex. We have, therefore, elected to chart a path midway between these approaches and construct a least-biased equilibrium statistical theory for convective mixing based on just the few physical constraints that define the heton ensemble in a natural manner as outlined in section 3.

b. Nonlinear stability for most probable statistical structures

The solutions to the Langevin mean-field equations are steady, exact solutions of the two-layer model in (2.1)–(2.3), which is easily demonstrated since the mean-field potential vorticities, \bar{q}_j , are functions of the mean-field streamfunctions [see, e.g., (4.8)]. In this section we apply the sufficient criterion developed in Mu et al. (1994, p. 176) for nonlinear stability of steady states in a two-layer quasigeostrophic fluid and show that there also exist equilibrium statistical states that are nonlinearly stable. This nonlinear stability condition

guarantees for inviscid dynamics that the enstrophy of perturbations for all later times is bounded by a fixed constant times the enstrophy of the initial perturbation; that is,

$$\sum_j \int (\delta\bar{q}_j)^2(t) \leq C \sum_j \int (\delta\bar{q}_j)^2(0). \quad (4.10)$$

The general conditions for nonlinear stability require that the streamfunctions, $\bar{\psi}_1$ and $\bar{\psi}_2$, be single-valued functions of the potential vorticities, \bar{q}_1 and \bar{q}_2 , for which we have an explicit representation, from (4.8), in the Langevin statistical theory:

$$\bar{\psi}_j = G_j(\bar{q}_j) = \frac{1}{\theta} \left(\frac{1}{Q_j} \mathcal{L}^{-1} \left[\frac{\bar{q}_j - \bar{Q}_j}{Q_j} \right] + \gamma_j \right), \quad j = 1, 2. \quad (4.11)$$

The criterion for nonlinear stability is expressed in terms of the derivative, G'_j , which we express in terms of the streamfunctions,

$$\begin{aligned} G'_j(\bar{q}_j)|_{\bar{q}_j = \bar{q}_j(\bar{\psi}_j)} &= \frac{1}{G_j^{-1'}} \\ &= \frac{1}{\theta Q_j^2} \frac{\sinh^2[Q_j(\theta\bar{\psi}_j - \gamma_j)] - [Q_j(\theta\bar{\psi}_j - \gamma_j)]^2}{\sinh^2[Q_j(\theta\bar{\psi}_j - \gamma_j)][Q_j(\theta\bar{\psi}_j - \gamma_j)]^2}. \end{aligned} \quad (4.12)$$

Notice that the sign of G'_j is determined by θ .

Upon applying the results of Mu et al. (1994), a solution to the two-layer quasigeostrophic Langevin statistical theory is nonlinearly stable if

- the vortex temperature is positive, $\theta > 0$
- the vortex temperature is negative, $\theta < 0$, and constants c_1, c_2, c_3, c_4 exist such that

$$\begin{aligned} -c_1 &\leq G'_1(r) \leq -c_2 < 0, & Q_{1-} < r < Q_{1+} \\ -c_3 &\leq G'_2(s) \leq -c_4 < 0, & Q_{2-} < s < Q_{2+} \end{aligned} \quad (4.13)$$

where the point formed from the upper bounds, (c_2, c_4) , lies within the area delimited by one branch of an hyperbola, which is defined by

$$\begin{aligned} &\left(-c_2 - \frac{\Lambda_B^{-1} + \Lambda_T^{-1}}{2} \right) + \left(-c_4 - \frac{\Lambda_B^{-1} + \Lambda_T^{-1}}{2} \right) \\ &< 0 \\ &\left(-c_2 - \frac{\Lambda_B^{-1} + \Lambda_T^{-1}}{2} \right) \left(-c_4 - \frac{\Lambda_B^{-1} + \Lambda_T^{-1}}{2} \right) \\ &> \left(\frac{\Lambda_B^{-1} - \Lambda_T^{-1}}{2} \right)^2. \end{aligned} \quad (4.14)$$

Here, Λ_B and Λ_T are the smallest eigenvalues of the

barotropic (Δ) and baroclinic ($\Delta - 2F$) operators, which, in a unit basin of finite deformation radius, are

$$\Lambda_B = -8\pi^2 \quad \Lambda_T = -8\pi^2 - 2F. \quad (4.15)$$

The conditions in (4.14) describe a region bounded by one branch of a family of hyperbolas, whose position depends on F . The region of stability is slightly larger for the larger values of F ; however, the gain in area is not practically significant.

5. Most probable states for the pure heton case

In this section we present the predictions of the equilibrium statistical theory for the spreading phase of a statistical ensemble of hetons distributed throughout a quiescent basin. Although the hetons are purely baroclinic and their placement is homogeneous, the maximum-entropy solution is typically an asymmetric monopole with roughly 90% of the energy budget being barotropic. The temperature anomaly, defined in (2.13), forms a relatively cool core that lies within the barotropic vortex, showing that hetons tend to cluster in the basin center, “governed” by the barotropic flow.

The scale of the vortices, both barotropic and baroclinic, are determined by two nondimensional length scales: L_ρ , the Rossby deformation radius, and $L_T \equiv \sqrt{\Delta\Gamma/\Delta Q}$, which is defined in section 3d and measures the density of hetons in the initial ensemble. For small values of these parameters, the statistical equilibrium flows establish a barotropic governor, a barotropic rim current that confines the temperature anomaly and suppresses baroclinic instability. As either of the length scales increases, both the barotropic and baroclinic vortices spread out. For sufficiently high L_ρ , the extent of the baroclinic vortex exceeds that of the barotropic vortex and the barotropic governor is lost. For increasing L_T , however, the barotropic governor remains in place and nonlinear stability is established for a large range of L_T .

Although the typical solution is an asymmetric monopole (within a reasonable energy range), there are three classes of large-scale structures that maximize entropy within different energy regimes. They are organized in the following symmetry groups:

- A “symmetric baroclinic monopole,” in which cyclonic and anticyclonic vortices, which are of equal strength, appear in different layers in the center of the basin (see, e.g., Fig. 6)

$$\begin{aligned} \bar{q}_1(x, y) &= -\bar{q}_2(x, y) \\ \bar{q}_j(x, y) &= \bar{q}_j(-x, y) \\ \bar{q}_j(x, y) &= \bar{q}_j(x, -y); \end{aligned} \quad (5.1)$$

the baroclinic monopole maximizes entropy at very low energies.

- An “asymmetric monopole” in which cyclonic or anticyclonic vortices, which are of differing strength,

appear in different layers in the center of the basin (see, e.g., Fig. 3)

$$\begin{aligned} \bar{q}_i(x, y) &= \bar{q}_j(-x, y) \\ \bar{q}_i(x, y) &= \bar{q}_j(x, -y); \end{aligned} \quad (5.2)$$

the asymmetric monopole maximizes entropy at low to moderate energies.

- A “diagonal pair” in which cyclonic and anticyclonic vortices, which are of equal strength, appear in different layers arranged diagonally (see, e.g., Fig. 7)

$$\bar{q}_1(x, y) = -\bar{q}_2(-x, -y); \quad (5.3)$$

the diagonal pair maximizes entropy at high energies.

This list is by no means exhaustive—we have found many other classes of solutions that exhibit even more restrictive types of symmetry. However, these additional types of solutions never maximize the overall entropy.

In order to calculate the equilibrium statistical heton structures that arise in a quiescent ambient flow, we must specify the maximum amplitude of the heton ensemble, ΔQ , the total circulation strength, $\Delta\Gamma$, and the total energy, E , in the basin. Upon substitution of the prior distributions in (3.12) for the heton ensemble, we solve the mean-field equations in (4.8) for the upper- and lower-layer streamfunctions. In this section we first show the maximum-entropy solutions for low density of hetons in the initial ensemble ($\Delta Q = 2.0$, $\Delta\Gamma = 0.15$) and small deformation radius ($F = 400$), and then examine the effects associated with changing both of the length scales associated with $\Delta\Gamma/\Delta Q$, and F .

a. Most probable statistical states with heton forcing and small Rossby deformation radius ($F = 400$)

The entropies for the entropy-maximizing classes of solutions listed in (5.1)–(5.3), that is, the baroclinic monopole, the asymmetric monopole and the diagonal pair, are shown in Fig. 2 for a range of energies at $F = 400$ and $L_T = 0.19$. We construct this diagram by solving the mean-field equations in (4.8) for a large number of prescribed energy values. Each such solution yields a most probable mean-field streamfunction, $\bar{\psi}$, and a set of Lagrange multipliers, θ and γ_j , from which the entropy, S in (4.3), is calculated via the one-point distributions, ρ_j in (4.7). The various classes of solutions are isolated by introducing the symmetries detailed above directly into the iterative algorithm described in section 4.

We find that the baroclinic monopoles maximize entropy at the very lowest values of energy in the “negative temperature” regime, in an interval too narrow to be visible in the diagram. Here, we refer to the vortex temperature, $1/\theta$ —to be distinguished from the physical temperature, $F\psi_T$ in (2.13)—which is simply a property of a changing volume of phase space for a given increase of energy. At energies immediately above the transition to negative vortex temperature, two higher-entropy clas-

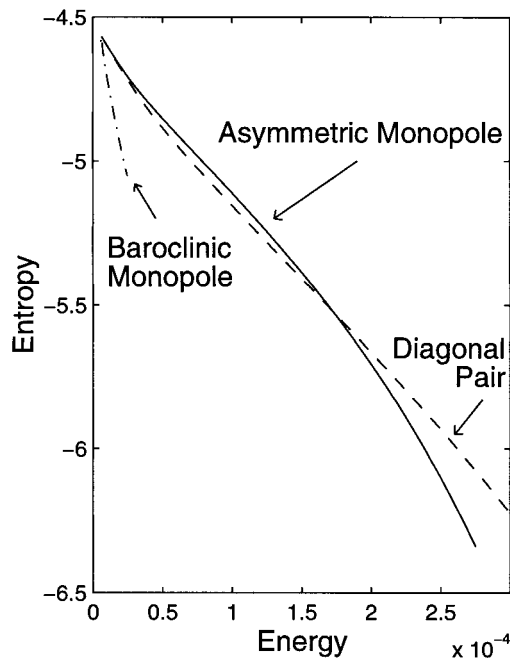


FIG. 2. Entropy–energy diagram showing the most probable solution classes for a homogeneous heton ensemble in quiescent ambient flow at small deformation radius ($F = 400$). The asymmetric monopoles (solid line) maximize the entropy for energies, $E \lesssim 0.00017$; the diagonal pairs (dashed line) for energies above this value. The branch of baroclinic monopoles (dash–dot line), from which the other two solution classes bifurcate, is the entropy maximizer in a very small interval of energy.

ses of solutions bifurcate from the branch of baroclinically symmetric solutions: 1) the asymmetric monopole, which bifurcates first, is the most probable state for energies, $E \lesssim 0.00017$, and 2) the diagonal pair, which bifurcates at a very slightly larger energy, is the most probable state for higher energies.

For this rather small value of L_T , only a small portion of these energy–entropy curves satisfies the criterion for nonlinear stability, defined in (4.14). The branch of solutions that represent asymmetric monopoles is provably nonlinearly stable up to the energy, $E = 0.000008$. The branch of solutions that represent diagonal pairs is provably nonlinearly stable up to the energy, $E = 0.000007$. We will see in section 5b, that the nonlinear stability criterion becomes much more useful as L_T increases. Also, in section 6 we show that the range of energies that satisfies the nonlinear stability criterion in (4.14) dramatically increases in the presence of a preexisting barotropic flow.

The Langevin statistical theory therefore predicts that, for a random bombardment of baroclinically symmetric hetons, the equilibrium most probable state has an asymmetric arrangement of potential vorticity between the two layers. In fact, nearly 90% of the energy budget in the equilibrium solutions is barotropic. At low to moderate energies the potential vorticity accumulates in the center of the domain, with a broader cyclonic

vortex in one layer and a more concentrated cyclonic vortex in the other. An example of a maximum-entropy asymmetric monopole is shown in Fig. 3, for $E = 0.000056$. In the case of quiescent initial conditions, these vortices may appear in either layer due to symmetry. An example with a more concentrated vortex in the upper layer and a broader vortex in the lower layer is depicted in the upper and lower velocity fields in the bottom two diagrams of Fig. 3. Here, and throughout the remainder of the paper, we show the conventionally defined barotropic and baroclinic streamfunctions, $\psi_B/\sqrt{2}$ and $\psi_T/\sqrt{2}$. The asymmetric monopole establishes, in the absence of any preexisting barotropic flow, its own barotropic governor. The extent of the barotropic streamfunction is broader than the baroclinic streamfunction, an effect illustrated by the relative positions of the streamlines shown in the two middle diagrams in Fig. 3. Since the temperature anomaly is proportional to the baroclinic stream field by (2.13), this shows that the heat in the statistical equilibrium solution accumulates in a compact region in the center of the basin.

The potential vorticity fields and streamfunctions of a maximum-entropy asymmetric monopole at a higher energy, for $E = 0.000156$, is shown in Figs. 4 and 5, respectively. In this case the potential vorticity fields approach the maximum values allowed by the statistical constraints, so the solution becomes nearly patchlike (see the potential vorticity plots in Fig. 10). This is seen in the barotropic and baroclinic portions of the potential vorticity fields, which are shown in Fig. 4. However, the barotropic streamfunction is again broader than the baroclinic component and so establishes a barotropic rim current that confines the baroclinic portion, and thus the heat anomaly, of the flow.

The baroclinic monopole is an overall entropy maximizer only at very small energies. However, by suitably restricting our maximum-entropy algorithm we may produce baroclinic monopole solutions. An example of an entropy-maximizer under the group of baroclinic symmetry from (5.1) is shown in Fig. 6, with energy $E = 0.00001$. The barotropic and baroclinic portions of the potential vorticity appear in the top two diagrams, and the upper- and lower-layer velocity fields appear in the lower two diagrams. The potential vorticity in this class of solutions is concentrated into a very compact baroclinic vortex that quickly approaches a patchlike solution. The pair of counterrotating vortices are aligned in the center of the basin, and the strength of the velocity field quickly drops off with the distance from the center of the domain. This is not the entropy-maximizing solution overall and obviously does not have any barotropic flow.

At higher values of energy, $E \gtrsim 0.00017$, the most probable equilibrium state is a diagonal pair, rather than the asymmetric monopole. Here, the asymmetry in the upper- and lower-layer potential vorticity fields is spatial: cyclonic and anticyclonic vortices separate into counterrotating pairs of equal strength located in op-

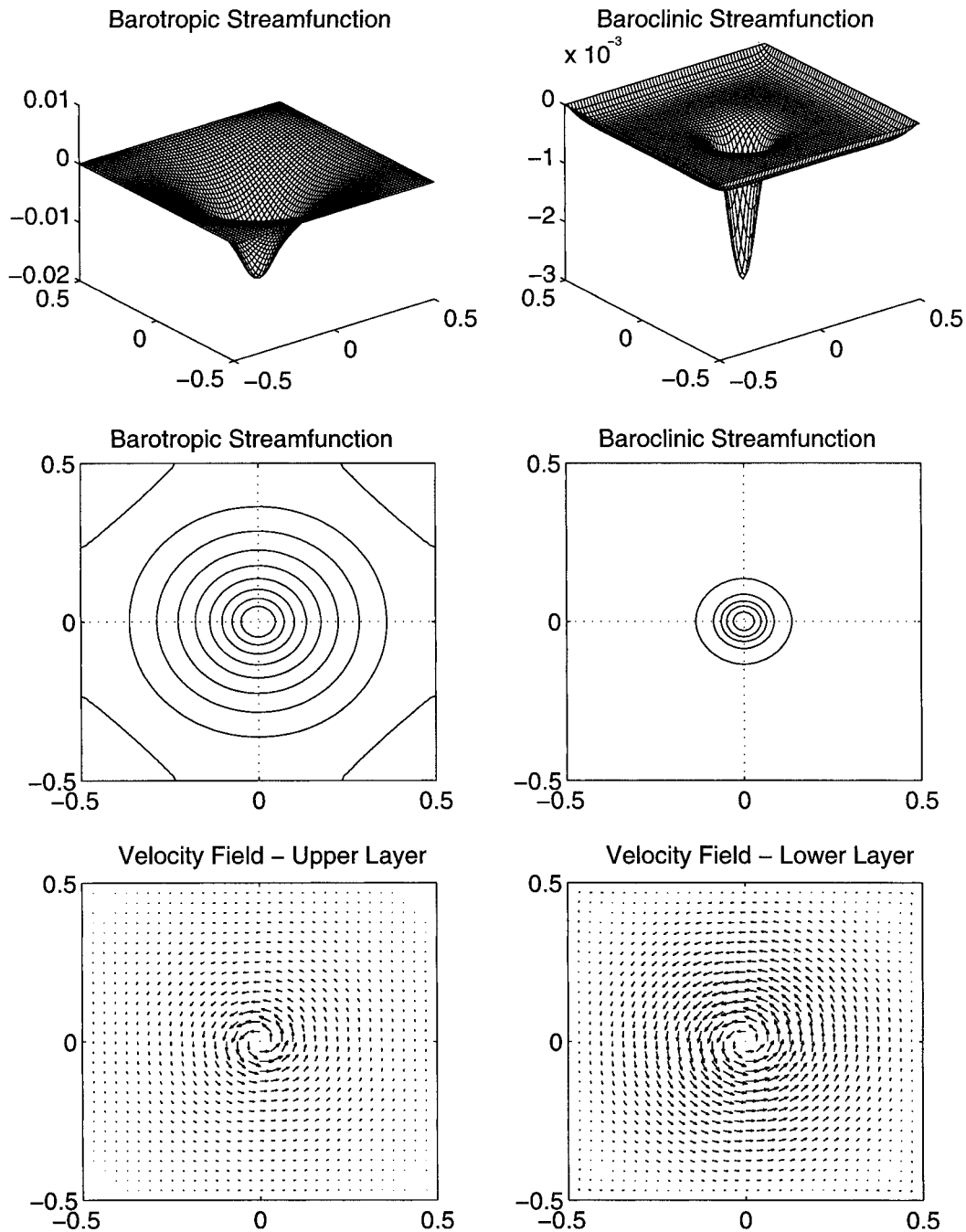


FIG. 3. Barotropic and baroclinic streamfunctions (top two rows) and the upper- and lower-layer velocity fields (bottom row) for the maximum-entropy asymmetric monopole for $F = 400$, $\Delta Q = 2.0$, $L_T = 0.19$, and $E = 0.000\ 056$.

posing corners of different layers. Thus, the equilibrium distribution of potential vorticity for spatially homogeneous heton forcing is aggregated into an opposing pair of coherent vortices. We note here that with the addition of a rather small ambient barotropic flow, as discussed in section 6b, the diagonal pair structure of

the entropy maximizer in this region is rapidly destroyed.

The two counterrotating vortices that form the diagonal pair each establish their own barotropic governors, which can be seen in the barotropic and baroclinic components of the potential vorticity fields and the

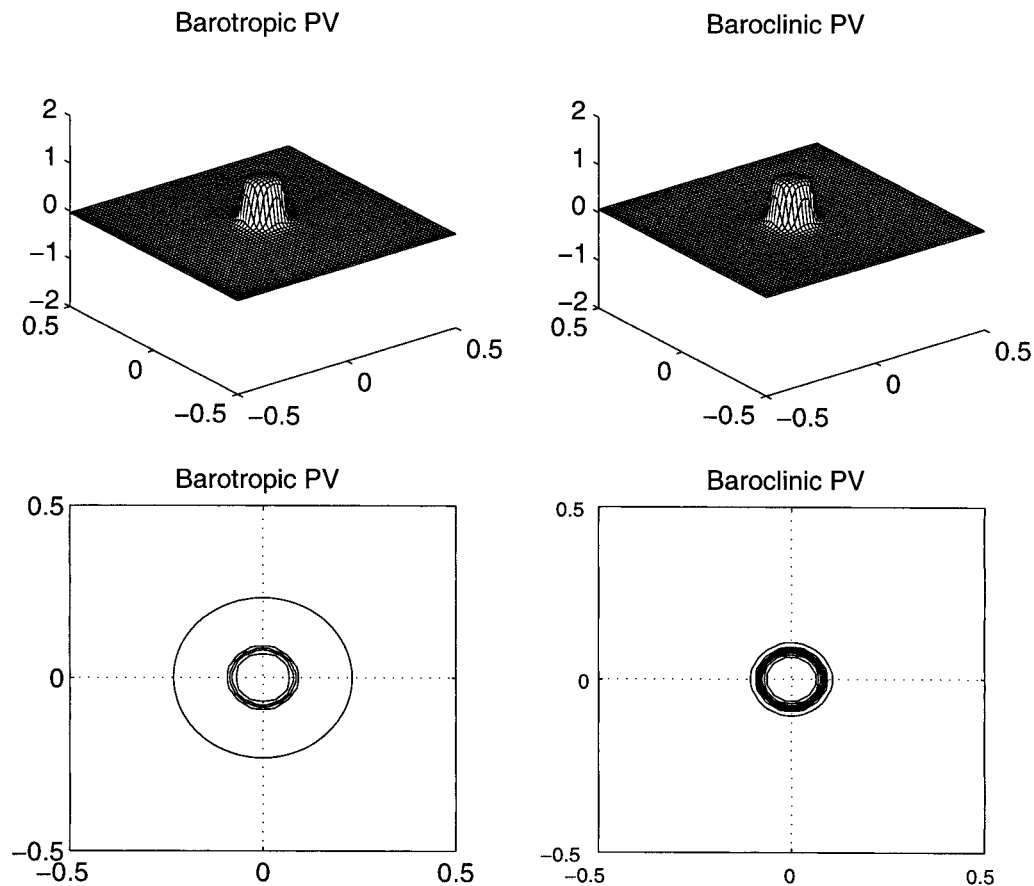


FIG. 4. Barotropic and baroclinic potential vorticity surfaces and contour lines for the maximum-entropy asymmetric monopole for $F = 400$, $\Delta Q = 2.0$, $L_T = 0.19$, and $E = 0.000156$. Notice that the vortices are nearly patchlike.

streamfunctions shown in Figs. 7 and 8. The energy in this example is $E = 0.000181$. The barotropic component of the streamfunction, visible in the diagrams in Fig. 8, form a cyclonic/anticyclonic pair of rim currents that confine the baroclinic portion of the flow. Here, the equilibrium heat distribution accumulates in two narrow regions confined to the centers of the counterrotating barotropic vortices.

The partition of the total energy among its three components, the barotropic, potential, and baroclinic kinetic portions of the energy defined in (2.9), is shown in Fig. 9. Additionally, we provide the ratio of baroclinic kinetic energy to the potential energy. Among the three major classes of solutions, the greatest differences are between those that have a barotropic component—the asymmetric monopoles and the diagonal pairs—and the one which does not—the baroclinic monopole. In fact, for small Rossby deformation radius ($F = 400$) the barotropic component of the energy is dominant, accounting for nearly 90% of the total energy in these two classes. It is striking that so much of the energy in the equilibrium state is barotropic when the underlying small-scale hetons are entirely baroclinic. This indicates that the

most probable statistical state predicts asymmetrical spreading in the two layers among hetons as in the calculations of Legg and Marshall (1993). The remainder of the energy is divided between the baroclinic components with the potential energy nearly four times greater than the baroclinic kinetic energy. Even in the case for the baroclinic monopole, in which all of the energy is baroclinic, the potential energy is the dominant component at small deformation radius.

b. Effect of heton density on most probable states

In this section we demonstrate the effect of increasing L_T without changing ΔQ , that is, effectively increasing the area of the basin that convectively overturns while preserving strength of the individual hetons, on the equilibrium statistical solutions. Both the barotropic and baroclinic portions of the flow spread out as the parameter approaches 0.5. As the flow extends to the basin scale, the portion of the energy that is barotropic decreases slightly and the stability of the solutions increases (at fixed values of energy and deformation ra-

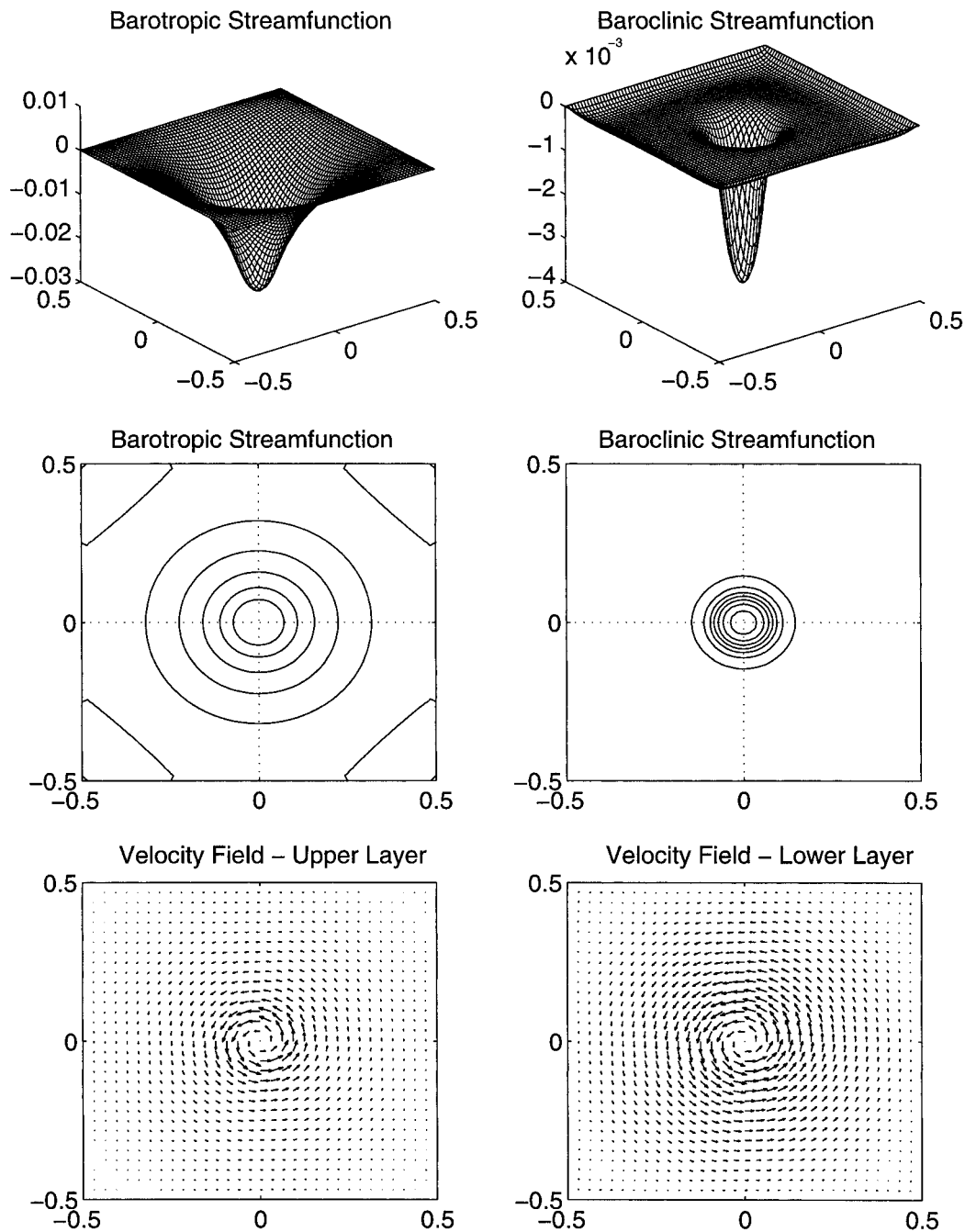


FIG. 5. Barotropic and baroclinic streamfunctions (top two rows) and upper- and lower-layer velocity fields for the asymmetric monopole described in Fig. 4. The baroclinic field is confined by the barotropic “governor,” which suppresses baroclinic instabilities.

dus), with nonlinear stability established for large enough L_T .

We increased the parameter L_T from 0.19 to 0.5 for asymmetric monopole and the diagonal pair solutions with energy, $E = 0.000\ 156$. No additional class of solutions maximizes the entropy, other than those listed in (5.1)–(5.3). At the lowest point in this range, a case

that is treated in section 5a, the maximum-entropy solution is an asymmetric monopole. Throughout this range the entropy of the asymmetric monopole exceeded that for the diagonal pair. Thus, increasing the heton strength does not generally induce a change of phase in the maximum-entropy solution.

The barotropic and baroclinic PV fields for the asym-

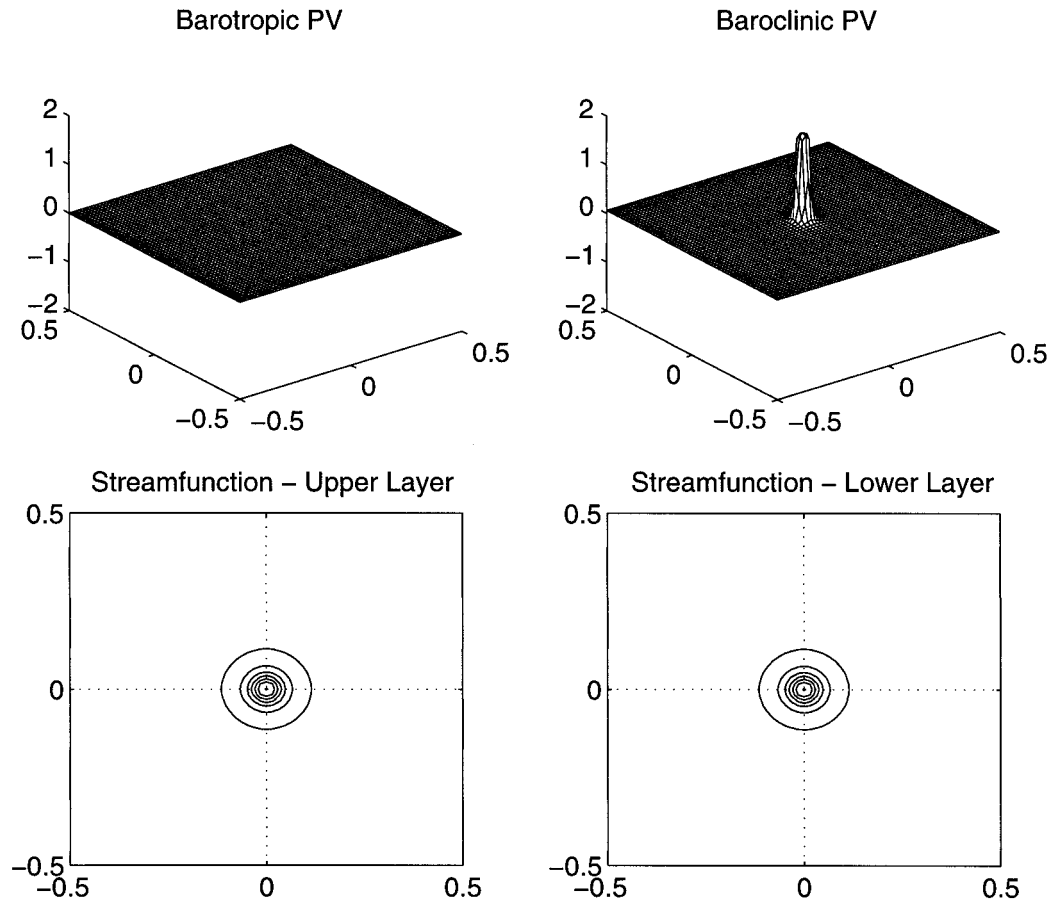


FIG. 6. Barotropic and baroclinic potential vorticity surfaces (top row) and contour lines for the barotropic and baroclinic streamfunction for the lower-entropy solution with baroclinic symmetry for $F = 400$, $\Delta Q = 2.0$, $L_T = 0.19$, and $E = 0.000\ 01$. Naturally, there is no barotropic part to the flow.

metric monopole are shown in Fig. 10 for $L_T = 0.19$, 0.27, and 0.39, which are the top, middle, and bottom two diagrams, respectively. The energy is held fixed at $E = 0.000\ 156$ and the deformation radius is determined by $F = 400$. The upper two PV fields are nearly patch-like. However, as the length scale L_T increases, both the barotropic and baroclinic components of the PV spread out. In each case the equilibrium solution establishes a barotropic governor, which circumscribes the baroclinic portion of the flow, although the barotropic rim current is quite broad in the lowest two diagrams.

The nonlinear stability criterion, in (4.14), is met for the equilibrium solution shown in the bottom two diagrams in Fig. 10—and for solution with larger values of L_T . The PV fields are quite spread out by this point, and both the barotropic and baroclinic portions are roughly the size of the domain. Notice that we have expanded the vertical scale in the bottom diagrams and that the baroclinic vortex is well confined by the barotropic rim current.

The temperature anomaly, which is proportional to the baroclinic streamfunction, is shown in Fig. 11 for $L_T = 0.19$, 0.27, and 0.39 at energy, $E = 0.000\ 156$.

An additional example is shown for a higher value of $L_T = 0.5$ and energy, $E = 0.0011$, in the bottom left-hand corner. The hetons cluster into a sharply localized peak in the center of the basin for the smallest value in the upper left-hand corner. The potential vorticity field is relatively flat in the region that surrounds the cold core. As the density of hetons in the initial ensemble increases, the magnitude of the anomaly decreases, the width of the core spreads, and the heat content in the surrounding flow increases, but remains uniformly distributed. We show the example in the bottom left-hand corner of the figure in order to demonstrate that a flow with a significant cool thermal anomaly in the basin center can be nonlinearly stable.

c. Effect of Rossby deformation radius on most probable states

By systematically decreasing the parameter F , we demonstrate the effects of the Rossby deformation radius on the equilibrium statistical solutions. As this length scale increases, the barotropic and baroclinic components of the equilibrium PV solutions, like those in

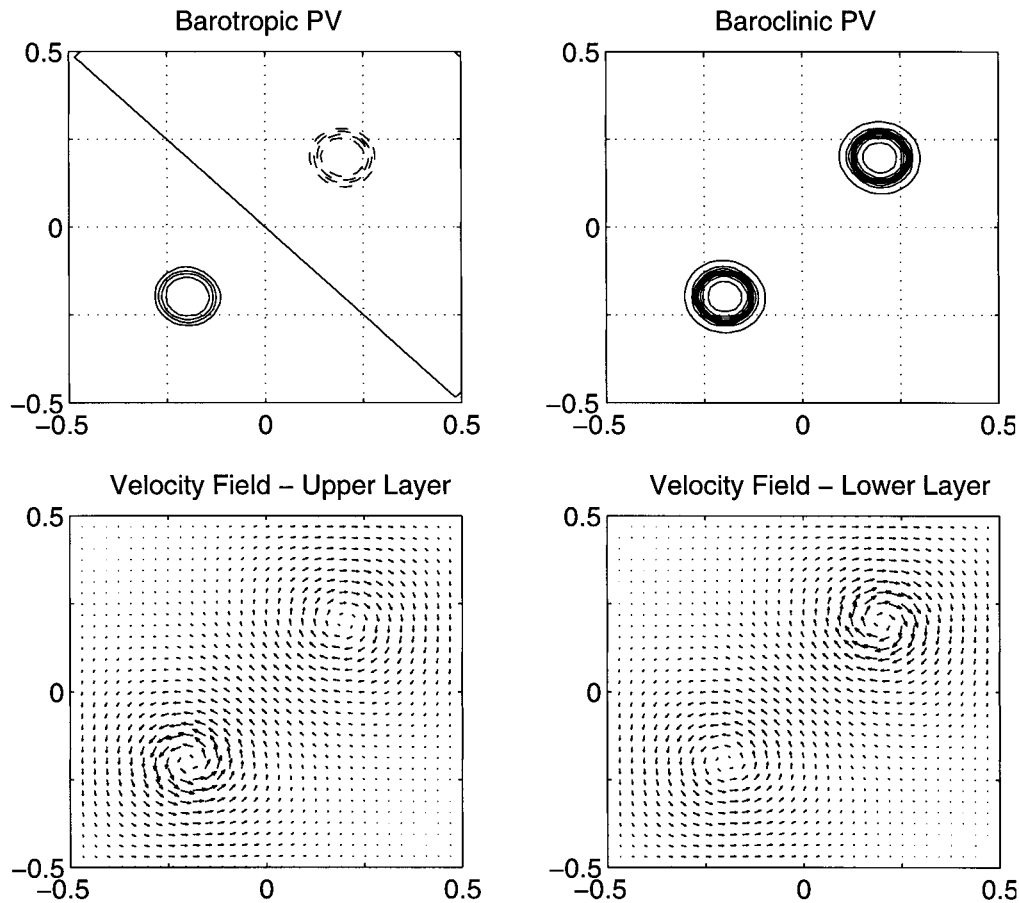


FIG. 7. Contour lines for the barotropic and baroclinic potential vorticities (top row) and velocity fields for the upper and lower layers (bottom row) for the maximum-entropy diagonal pair for $F = 400$, $\Delta Q = 2.0$, $L_T = 0.19$, and $E = 0.000\ 181$. The positive (negative) contours of the barotropic potential vorticity are drawn in solid (dashed) lines.

section 5b, broaden in shape. Unlike the previous examples, however, at the largest deformation radius considered, which corresponds to $F = 4$, the barotropic flow does not confine the barotropic vortex, so no circumscribing rim current is formed. This is related to the relative decoupling of the two layers that occurs for small values of F , in which the energy in the barotropic portion of the flow drops to a maximum of 30%.

The effects of decreasing F are shown in the entropy–energy diagrams shown in Figs. 12a and 12b, which correspond to $F = 4$ and 40, respectively. The density of the heton ensemble is held fixed at $\Delta Q = 2.0$ and $L_T = 0.19$. Qualitatively, the diagrams are quite similar to each other and to the entropy–energy diagram shown in Fig. 2 for $F = 400$. Three classes of solutions maximize the entropy within three disjoint intervals of energy. At the lowest energies, the symmetric baroclinic monopole class of solutions is the entropy maximizer. A bifurcation point appears in the diagrams; for energies above this point the asymmetric monopole class of solutions is the most probable. At slightly higher energy the diagonal pair solutions bifurcate from the symmetric

monopoles, but with lower entropy than the asymmetric monopoles. At some large value of energy, one vortex in the asymmetric monopole approaches a vortex patch and rapidly drops in entropy. At this point there is a transition in each of the energy–entropy diagrams and the diagonal pair is the maximum-entropy solution at higher energies.

The families of curves in Figs. 12a and 12b nearly coincide so that, for $F = 4$, it is difficult to separate the various solution branches by eye. In fact, the bifurcations of the asymmetric monopoles and the diagonal pairs appear at relatively higher values of energy as the deformation radius increases. All of the provably nonlinearly stable equilibrium states for $F = 4$, which inhabit a relatively very narrow interval, exhibit baroclinic symmetry.

The overlapping of the entropy curves for large deformation radius implies a blurring of the distinctions between the various solution classes. Indeed, this can be seen in the energy diagrams shown in Fig. 13 for $F = 4$. The barotropic component is relatively small, never rising above 30% of the total energy. The bifurcation

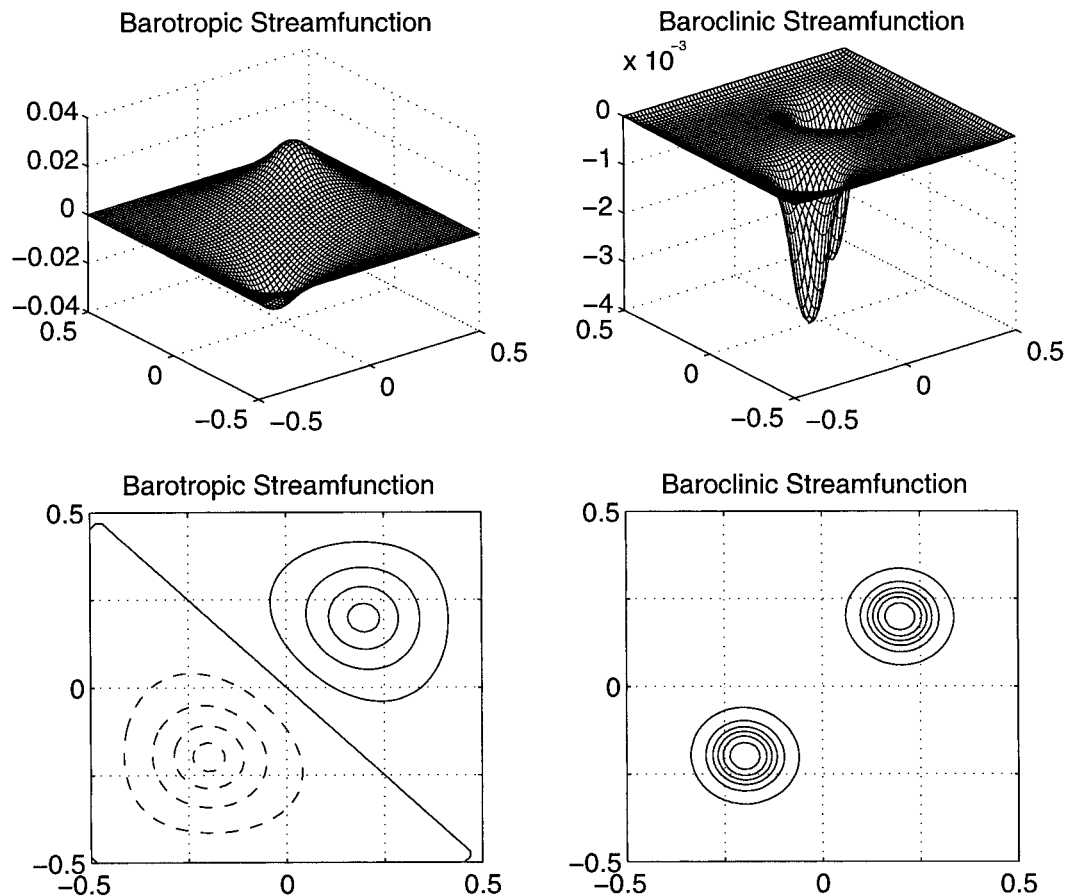


FIG. 8. Barotropic and baroclinic streamfunctions for the maximum-entropy diagonal pair described in Fig. 7. Notice that the baroclinic streamlines are tightly confined within the cores of the barotropic vortices. The positive (negative) contours of the barotropic streamfunction are drawn in solid (dashed) lines.

of the asymmetric monopoles and diagonal pairs from the baroclinically symmetric branch is easily seen here. The solutions for large Rossby deformation radius are therefore largely baroclinic, with the baroclinic kinetic component, between 60% and 80% of the total energy budget, being dominant.

The weakening of the barotropic component of the total energy leads to the loss of the barotropic governor in the equilibrium flow. The barotropic and baroclinic streamfunctions for an asymmetric monopole and a diagonal pair are shown, in Figs. 14 and 15, for $F = 4$ and $L_T = 0.19$. In both examples the baroclinic streamfunction is broader in extent and greater in magnitude than the weaker barotropic component. Notice that the counterrotating vortices in the diagonal pair are quite close, being drawn together at small F . There is no barotropic rim current here; the velocity fields in the upper and lower layers, shown in the bottom two diagrams of these figures, rotate in the opposite sense to one another—cyclonic in the upper layer, anticyclonic in the lower layer. The velocity fields occupy nearly complementary regions of the domain for the asymmetric monopole and are nearly coincident in the di-

agonal pair but, either way, the baroclinic portion of the flow is dominant.

The temperature anomaly, which is proportional to the baroclinic streamfunction, is strongly affected by the increase in deformation radius. This is shown in Fig. 16, for three maximum-entropy solutions at $F = 4, 40,$ and 400 . The allowable range of energy is widely different in these three cases: in order to compare the effect of the deformation radius, we have used the transition point between asymmetric monopoles and diagonal pairs in the energy-entropy diagrams as a common signpost. The three maximum-entropy asymmetric monopoles have energies just below this point. The extent of the heat anomaly decreases sharply with the decrease in the deformation radius, and the magnitude of the anomaly increases as \sqrt{F} .

The scale of the equilibrium solutions is ruled by two length scales—the deformation radius, $L_p = 1/\sqrt{F}$, and a length scale, $L_T = \sqrt{\Delta\Gamma/\Delta Q}$, which is determined by the density of hetons in the initial ensemble. The equilibrium configuration of hetons, at least for the quiescent initial case, tends to accumulate in a cool thermal anomaly in the center of the basin, circumscribed by a baro-

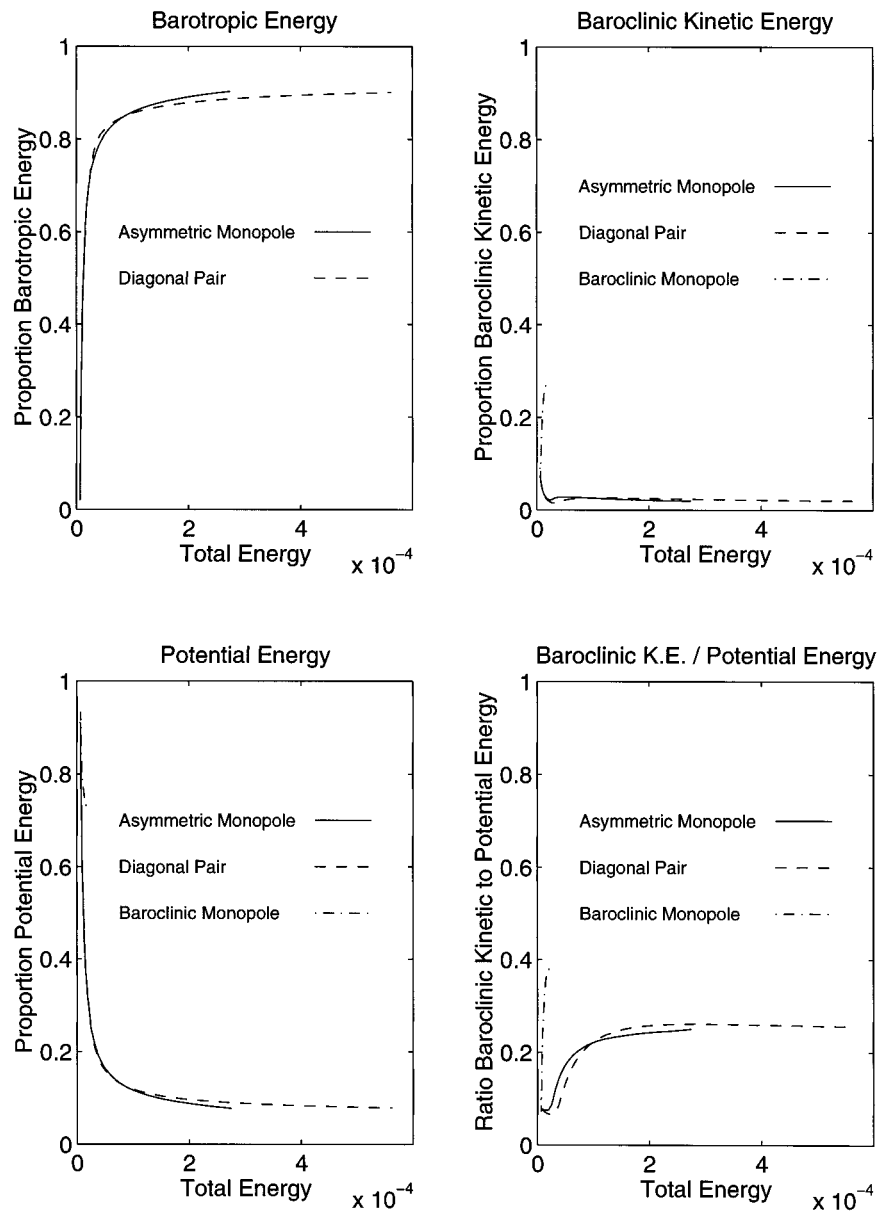


FIG. 9. The energy budget for the maximum-entropy solutions shown in Fig. 1 for $F = 400$ and $L_r = 0.19$: (a) barotropic energy, (b) baroclinic kinetic energy, (c) potential energy, and (d) the ratio of baroclinic kinetic to potential energies.

tropic rim current for small values of *both* parameters. In the absence of any barotropic preconditioning, the maximum-entropy solutions establish their own barotropic governors. As either of the length scales increases, however, the barotropic component of the energy weakens and PV structures broaden. However, for $L_p \ll 1$, the overall energy remains overwhelmingly barotropic and a rim current confines the temperature anomaly. In contrast, in the case of very large deformation radius the barotropic portion of the flow weakens considerably and no longer governs the baroclinic vortex that occupies the center of the basin.

6. Most probable states for hetons in a barotropic environment

In section 5 we calculated and discussed the maximum-entropy structures that arise in a quiescent basin subject to a random placement of hetons throughout the basin. Here, we study the large-scale structures produced by a statistical ensemble of hetons spread uniformly in a preexisting ambient barotropic flow. We distinguish between two cases:

- the strength of the barotropic initial flow is much

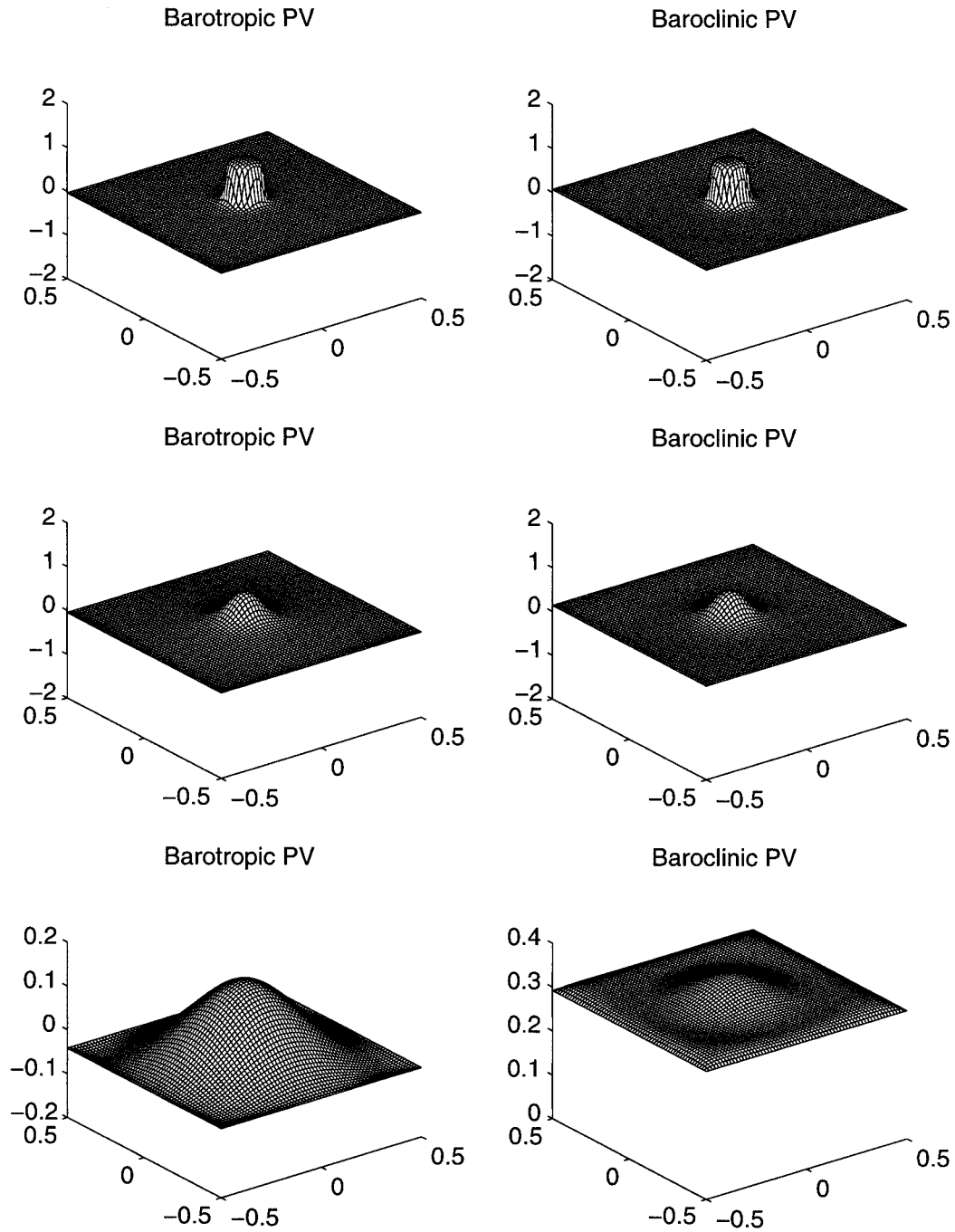


FIG. 10. Barotropic and baroclinic potential vorticity surfaces for $F = 400$, $\Delta Q = 2.0$, $E = 0.000\ 156$, and $L_T = 0.19$ (top row); 0.27 (middle row); and 0.39 (bottom row). The last example is nonlinearly stable. Notice that the scale has been magnified to show the structure of the potential vorticity fields in the bottom diagrams.

- greater than the strength of the hetons—a strong preconditioned barotropic flow, ($Q_B \gg \Delta Q$)
 - the strength of the barotropic initial flow is weaker than the strength of the hetons—a weak preconditioned barotropic flow, ($Q_B < \Delta Q$).
- In contrast to the results of the previous section, the

barotropic preconditioning of the flow leads to a single class of entropy-maximizing solutions, which exhibit the symmetries of the asymmetric monopole defined in (5.2). The addition of a barotropic component to the initial flow tends to increase nonlinear stability and helps to reinforce the barotropic governor that estab-

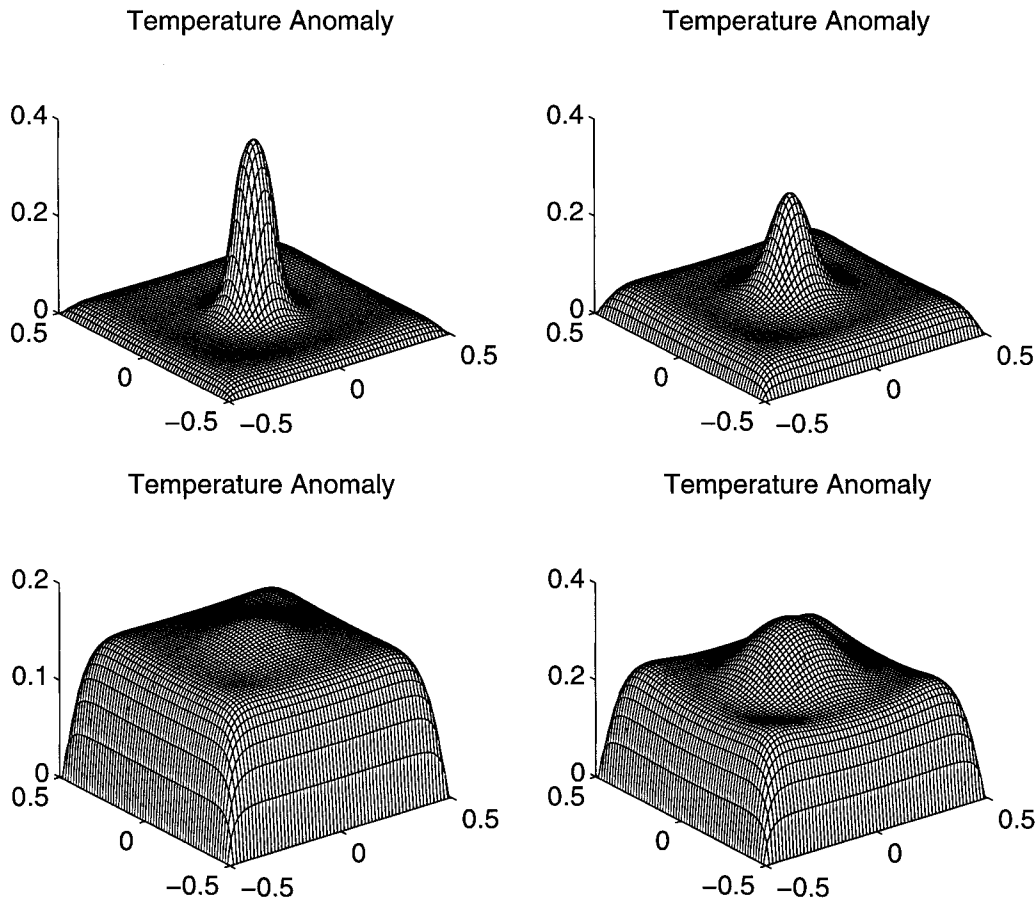


FIG. 11. Temperature anomalies for the asymmetric monopoles with $F = 400$, $E = 0.000\ 156$, and $L_T =$ (a) 0.19, (b) 0.27, (c) 0.39. The final example in (d) has $E = 0.0011$ and $L_T = 0.5$. The two examples in the bottom row are both nonlinearly stable.

lishes a rim current that confines the temperature anomaly. Typically, more than 95% of the energy in the flow is barotropic.

Maximum-entropy structures for ambient flow with barotropic preconditioning are naturally barotropic. They are calculated by specifying the vorticity interval, Q_B , and large-scale circulation, Γ_B , for the upper and lower layers (introduced in section 3c) and solving the mean-field equations for a given energy. The PV structure is identical in the upper and lower layers, forming a cyclonic monopole vortex in the center of the basin. The scale of the vortex is dependent upon the quantity, Γ_B/Q_B , which defines a barotropic length scale analogous to L_T^2 . We hold this parameter fixed at $\Gamma_B/Q_B = 0.075$. At very high energies, the barotropic monopoles become patchlike.

Maximum-entropy solutions for an ensemble of hetons distributed in an ambient flow with barotropic preconditioning require that all of the parameters introduced in section 3c be specified: the barotropic vorticity interval Q_B , and large-scale circulation, Γ_B , and the heton vorticity amplitude, ΔQ , and total heton circulation strength, $\Delta\Gamma$. Once the energy is specified, the total

circulations in the upper and lower layer in (3.15) are calculated, and the mean-field equations in (4.9) are solved.

a. Strong preconditioned barotropic flow

The most probable states for a statistical ensemble of hetons placed in an ambient flow with strong barotropic preconditioning establish strong barotropic governors and, at fixed energy, are more likely to be nonlinearly stable than comparable structures that arise in quiescent flow. In this section, we contrast two most probable solutions in which the deformation radius is small, $F = 400$, the energy is held constant at $E = 0.000\ 435$, and the barotropic flow is strongly preconditioned, $Q_B/\Delta Q = 10$: one which is purely barotropic and one in which the density of the heton ensemble has achieved its maximum for the given heton strength, that is, $\Delta\Gamma/\Delta Q = 1$.

The barotropic and baroclinic streamfunctions for these two cases appear in Fig. 17. Naturally there is no baroclinic part to the purely barotropic flow, so this is not displayed. However, comparison of the barotropic streamlines, which lie on the left-hand side of the figure,

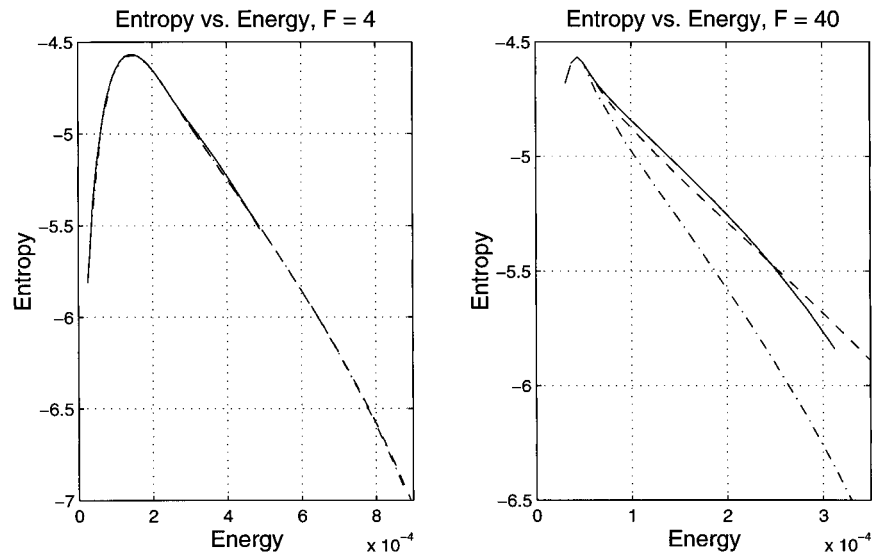


FIG. 12. Entropy–energy curves for the most probable solutions for (a) $F = 4$ and (b) $F = 40$. The solution branches nearly overlap at large deformation radius, however, the relative ordering of their entropies does not change (also, see Fig. 1). The asymmetric monopole solutions are shown in solid line, the diagonal pairs in dashed line, and the baroclinic monopoles in dash–dot line.

shows that there is practically no change in the barotropic structure even as the statistical ensemble of hetons achieves its maximum density. The portion of the energy that remains barotropic in this case is overwhelming—greater than 99% of the total budget. Both of these examples are nonlinearly stable by the criterion in (4.14).

The strongly preconditioned barotropic flow establishes a barotropic governor under the random placement of hetons throughout the domain. The streamlines of the baroclinic part are concentrated in the center of the basin, well circumscribed by the barotropic rim current. In fact, the thermal anomaly forms a relatively cool region in the center of the basin, which is shown in the upper right-hand portion of Fig. 17. In the spreading phase of open-ocean convection, the statistical theory predicts that a spatially homogeneous ensemble of hetons tends to coalesce in the core of the barotropic vortex, forming a stable, cool temperature anomaly confined to the basin center.

b. Weak preconditioned barotropic flow

Here, we examine the equilibrium statistical structures that arise in a relatively weak preexisting barotropic vortex, where the strength of the preconditioned flow is less than the strength of the ensemble of hetons. We show that the barotropic preconditioning tends to increase the nonlinear stability of the maximum-entropy asymmetric monopoles (as compared to the quiescent initial conditions) and that, for a low density of hetons in the initial ensemble ($\Delta Q = 2.0$, $L_T = 0.27$), a preexisting weak barotropic flow tends to promote a con-

centration of cold anomalies toward the basin edges upon adding hetons in response to a cold air outbreak. The barotropic component of the flow dominates the total energy, increasing from roughly 90% to 95% of the budget, even for weak preconditioning, $Q_B/\Delta Q = 0.08$.

We show the barotropic and negative of the baroclinic (for reasons of visual clarity) streamfunctions in Fig. 18 for an asymmetric monopole defined by $E = 0.000156$ and $L_T = 0.27$, for small deformation radius with $F = 400$, at three different levels of barotropic preconditioning. The upper, middle, and bottom two diagrams are for $Q_B/\Delta Q = 0, 0.04$, and 0.08 , respectively, which shows that the preconditioning is quite weak in all three cases.

The barotropic vortex, which is cyclonic, broadens as the barotropic preconditioning increases. The baroclinic portion of the flow also broadens, although the extent of the baroclinic vortex spreads at a slower rate. The magnitude of the baroclinic vortex decreases considerably—decreasing by a factor of three—since the barotropic preconditioning induces a concentration of cold anomalies toward the edges of the basin. However, it is interesting to note that the barotropic portion of the flow continues to govern the cold anomaly that remains in the basin center. The relative increase in the barotropic part of the flow can be measured by the increase in the barotropic component of the energy, which rises from 90% to 95% of the total energy budget as $Q_B/\Delta Q$ increases from 0 to 0.08.

The structure of the temperature anomaly is shown in baroclinic streamfunctions, which lie on the right-hand side of Fig. 18. The hetons, confined to the center

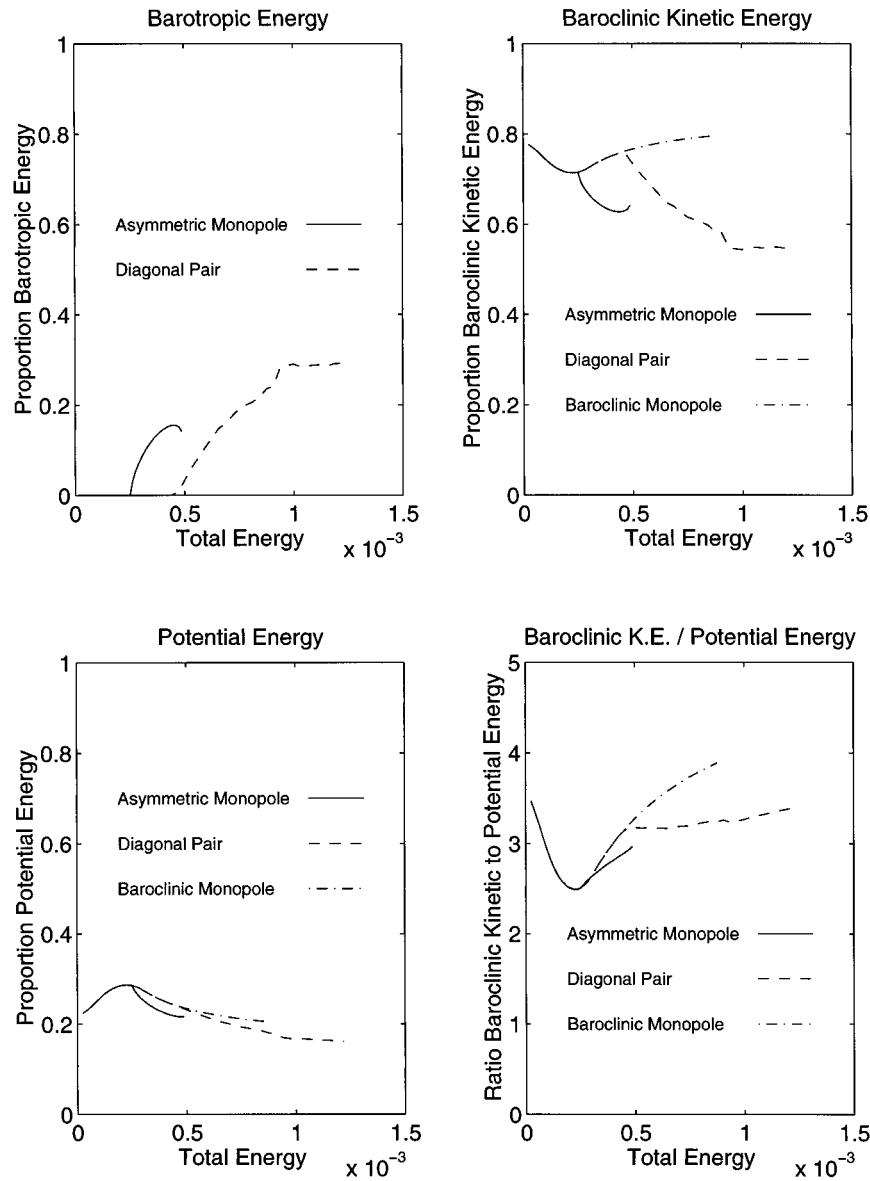


FIG. 13. The components of the energy as in Fig. 9 at large deformation radius, $F = 4$.

of the domain in the limit of quiescent flow, tend to spread in extent and lessen in magnitude as the barotropic preconditioning increases. The temperature anomaly is greatest in the basin center for the top two cases with $Q_B = 0$ and 0.04. However, by the point $Q_B = 0.08$, the aggregation of hetons in the basin center is reduced to a mere dimple in the temperature surface, and the hetons tend to cluster in the four corners of the square domain.

The increase in barotropic preconditioning stabilizes the equilibrium flow. Indeed, the maximum-entropy solution shown in the bottom two diagrams in Fig. 18 is nonlinearly stable, as are all solutions with stronger barotropic preconditioning. This trend coincides with the increase in the barotropic component of the energy,

which approaches nearly 95% of the total energy in the flow. Forcing a weakly preconditioned barotropic flow by randomly placed hetons yields an equilibrium statistical configuration that 1) is more stable, 2) has a greater portion of barotropic energy, and 3) increases the anticyclonic rotation of the baroclinic part, in comparison to the pure heton case examined in section 5.

7. Summary and concluding discussion

A “most probable state” equilibrium statistical theory for the spreading phase of open-ocean convection has been introduced and developed in sections 3 and 4 of this paper within the context of heton models for two-layer quasigeostrophic flow. The “most probable”

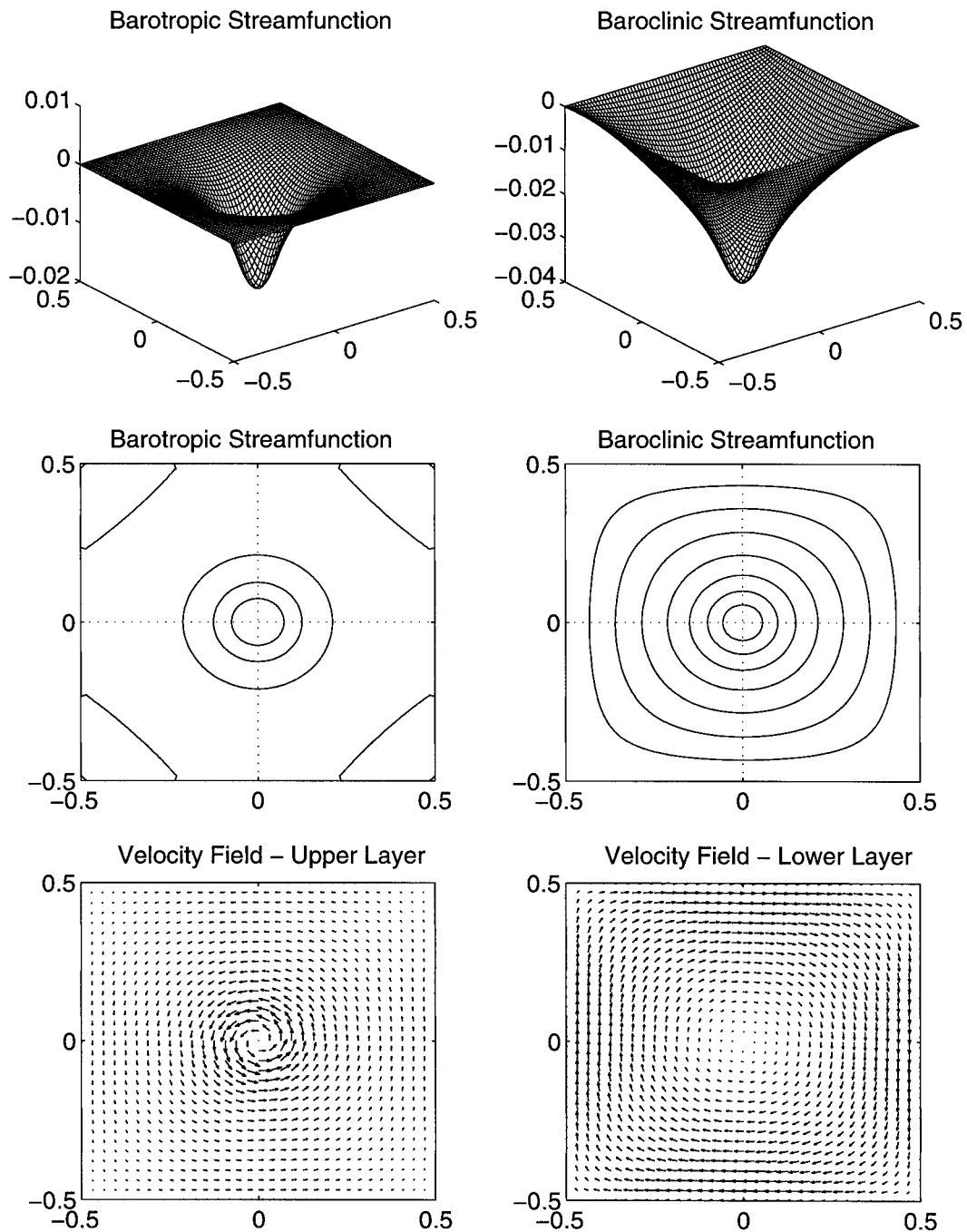


FIG. 14. Barotropic and baroclinic streamfunctions (top two rows) and the velocity fields for the upper and lower layers (bottom row) for the maximum-entropy asymmetric monopole at $L_T = 0.19$ and $F = 4$. Notice that the baroclinic vortex is no longer confined by the barotropic component of the flow.

equilibrium statistical states at large times arising from a basinwide cooling event are predicted through a maximum-entropy principle involving only a few conserved quantities for the inviscid dynamics: energy, circulation, and extrema for potential vorticity in each layer. As discussed in section 3, these statistical theories predict the coarse-grained mean-field response to a random

cooling event over the entire basin as represented by a random heton distribution with a prescribed maximum amplitude, ΔQ , and circulation anomaly, $\Delta \Gamma$. In this paper it is established that the nondimensional parameter L_T , introduced in (3.7), which measures the patchiness of the cooling event has a critical role in determining the structure of the most probable statistical state.

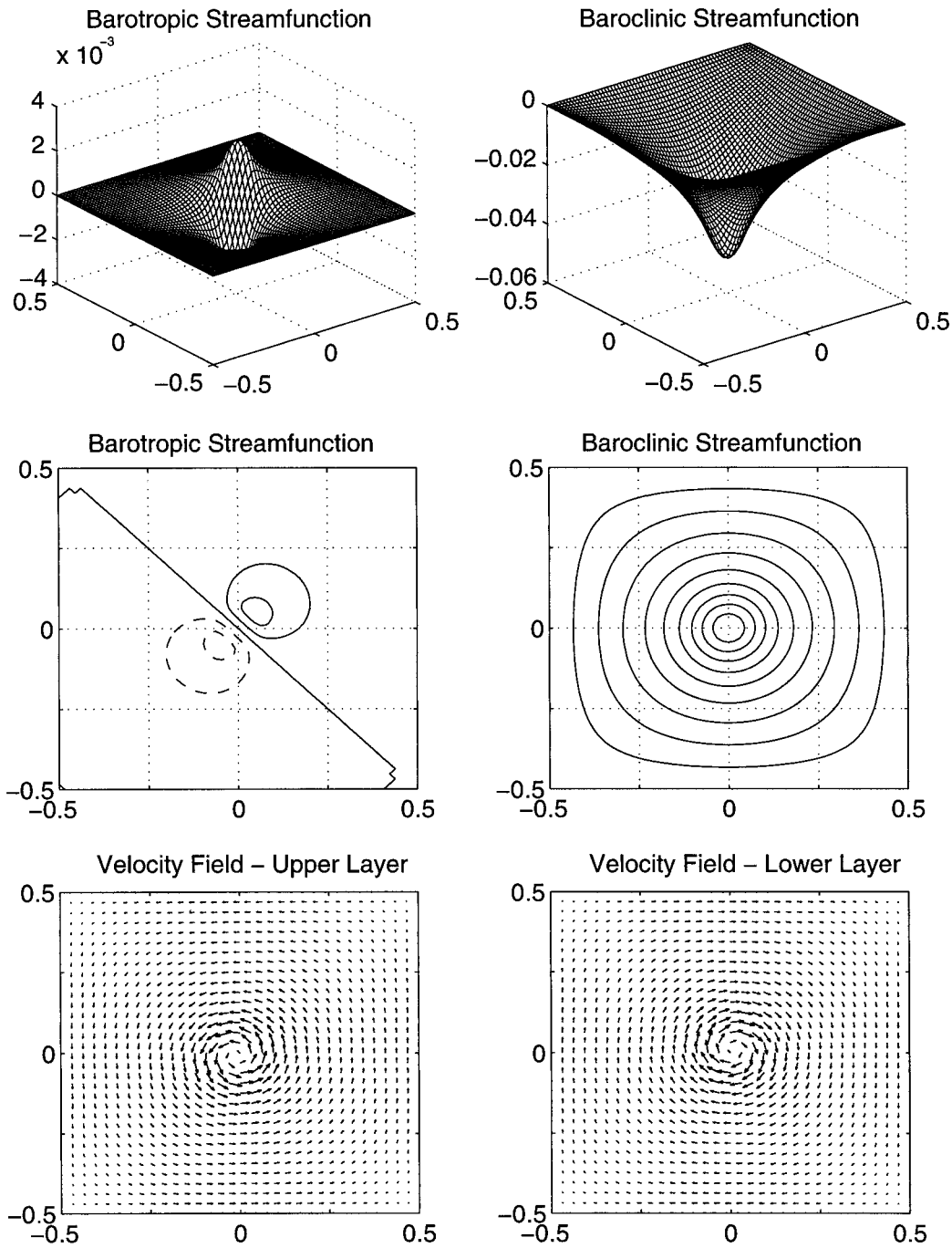


FIG. 15. Barotropic and baroclinic streamfunctions (top two rows) and the velocity fields for the upper and lower layers (bottom row) for the maximum-entropy diagonal pair at $L_T = 0.19$ and $F = 4$. As compared to the streamlines in Figs. 7 and 8, the counterrotating vortices are quite close to one another. The positive (negative) contours of the barotropic streamfunction are drawn in solid (dashed) lines.

The predictions of the statistical theory for quiescent flow in a rectangular basin are presented in section 5. For the situation with a small Rossby deformation radius compared to the basin scale, $F = 400$, the typical most probable states are asymmetric monopoles with the

overwhelming energy contribution being barotropic (85%–90% of the energy budget) and the temperature anomaly confined within the region of strong barotropic flow. Thus, the statistical theory automatically predicts a confined cold-temperature anomaly, governed by a

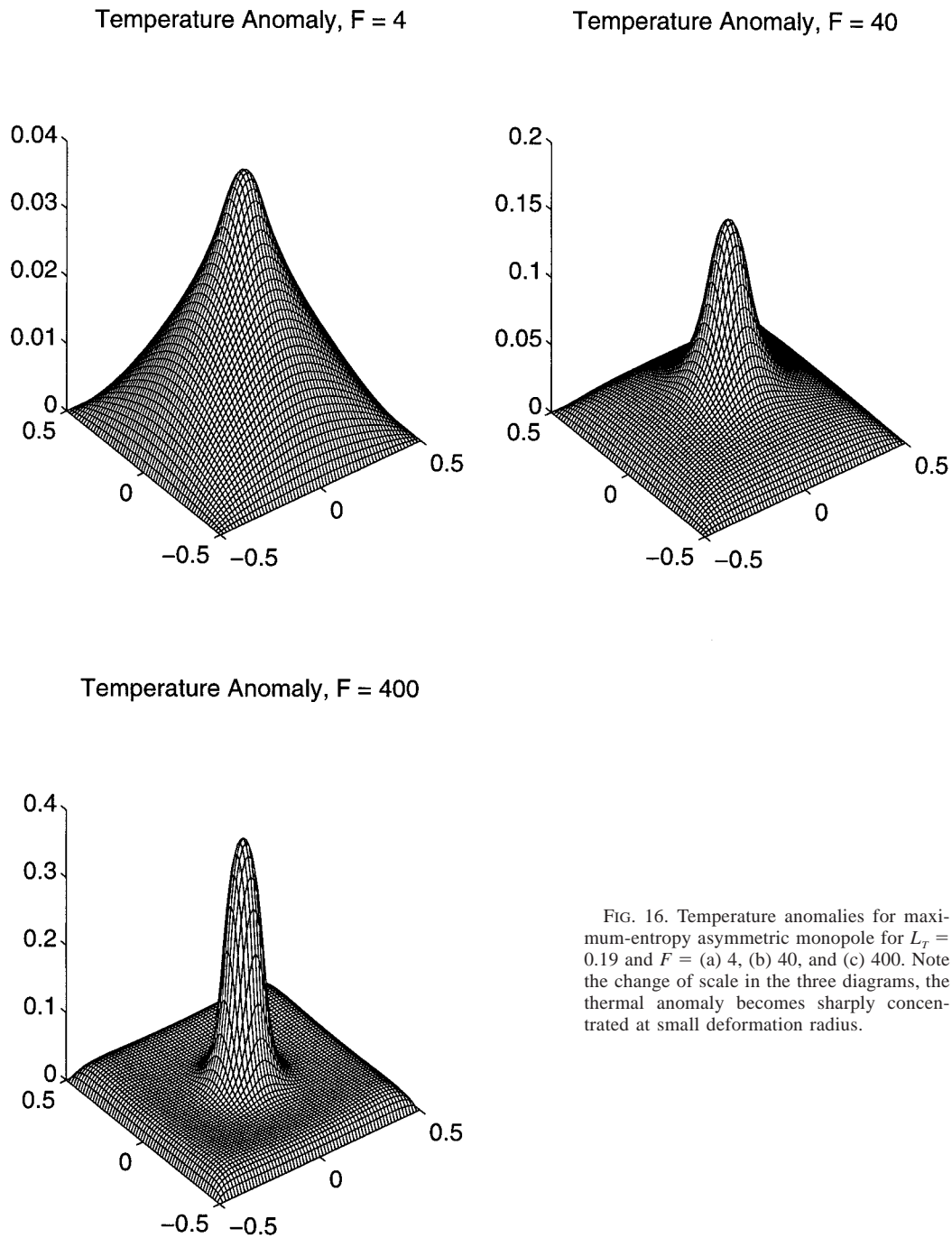


FIG. 16. Temperature anomalies for maximum-entropy asymmetric monopole for $L_T = 0.19$ and $F =$ (a) 4, (b) 40, and (c) 400. Note the change of scale in the three diagrams, the thermal anomaly becomes sharply concentrated at small deformation radius.

sheared, barotropic rim current. Furthermore, the parameter L_T measures the spread of the baroclinic core of the most probable state. A qualitatively similar structure—stable baroclinic core surrounded by a barotropic flow—appears in the numerical integration of heton models (Legg and Marshall 1993; Legg et al. 1996), although on very different spatial and temporal scales. However, the dynamical heton studies yield insight into the production and maintenance of a single convective

tower; the equilibrium statistical theory in the current paper yields predictions for the ultimate mixing of many such towers that form in a basinwide surface cooling event.

As described in section 5b, the nonlinear stability of this predicted structure for fixed energy depends crucially on the size of the nondimensional parameter L_T with larger values yielding stability. The effect of a much larger Rossby deformation radius on the predic-

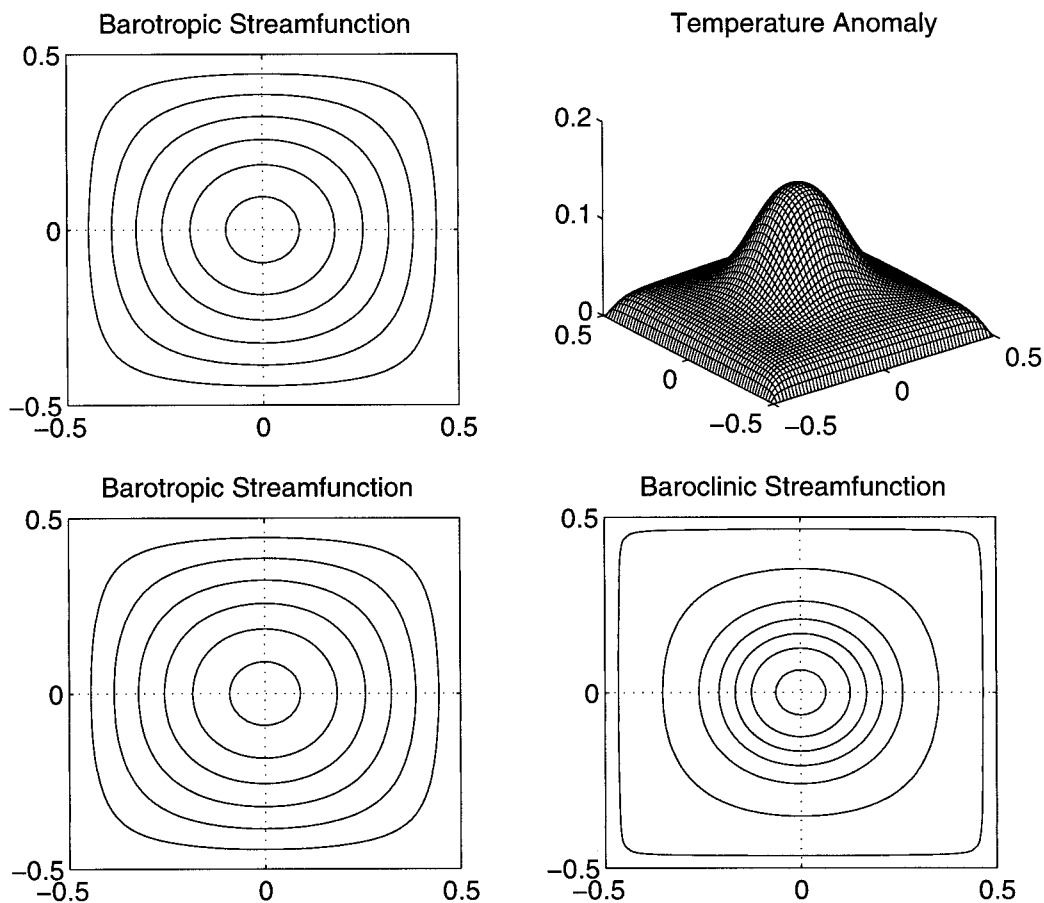


FIG. 17. Barotropic and baroclinic streamlines for the ambient flows with strong barotropic preconditioning at small Rossby deformation radius ($F = 400$). (a) The flow is entirely barotropic, so the baroclinic part is not shown. (c) and (d) the baroclinic and barotropic streamlines shown for a heton ensemble with maximum density, $\Delta\Gamma/\Delta Q = 1$ is added to the barotropic flow. Notice that the barotropic streamlines register no change and the baroclinic streamlines are strongly confined. Both flows are nonlinearly stable. The temperature anomaly for the strongly preconditioned flow with $\Delta\Delta/\Delta Q = 1$ is shown in (b).

tions of the statistical theory is presented in section 5c; for larger values such as $F = 4$, in contrast, most of the energy is baroclinic and the temperature anomaly is spread throughout the domain with a larger scale than that for the barotropic flow.

In section 6 the predictions of the statistical theory are developed for the important situation in which a statistical ensemble of hetons mimicking a cooling event is added to a preexisting ambient barotropic flow in the basin. Both the examples with strong and weak barotropic flow point to the role of the “barotropic governor” (James 1987; Nakamura 1993) in stabilizing these flows with a confined temperature anomaly.

The statistical theory we utilize here, based on a few constraints, yields completely different and fully nonlinear predictions of most probable states when compared with the standard energy–entropy statistical theory (Salmon et al. 1976). On the other hand, the energy–

entropy statistical theory has had some success in parameterizing features of topography, such as topographic stress (Holloway 1992; Cummins and Holloway 1994). The authors plan to explore the use of the fully nonlinear equilibrium statistical theory for the spreading phase of open-ocean convection, developed here as a crude parameterization of open-ocean convection, in numerical general circulation models.

Basin topography plays a significant role in the preconditioning for open-ocean convection (Hogg 1973; Alverson and Owens 1996; Madec et al. 1996). An important future research direction is the influence of topography on the predictions of the equilibrium statistical theory as well as more general preexisting basin-scale flows. Another important research direction within the context of the two-layer models presented here involves the realizability and metastability of these equilibrium statistical steady states with damping and forcing representing wind stress. Such studies have already been

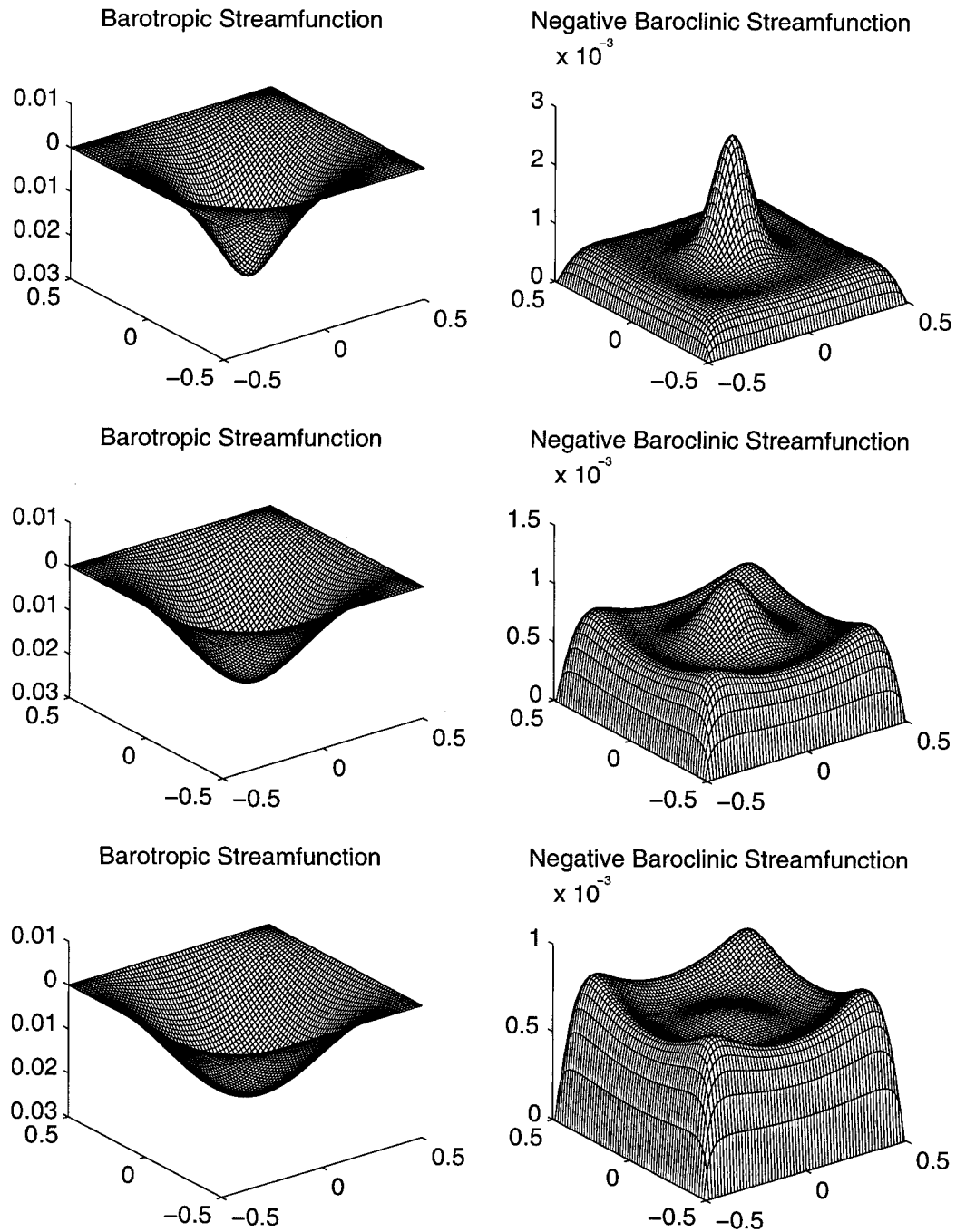


FIG. 18. Barotropic and (negative) baroclinic streamfunction surfaces for ambient flows with weak barotropic preconditioning at small Rossby deformation radius ($F = 400$). The ratio of the amplitudes of the ambient barotropic to heton portion of the total flow is $Q_B/\Delta Q = 0.0$ (top row), 0.04 (middle row), and 0.08 (bottom row). The negative of the barotropic streamfunctions is proportional to the temperature anomaly.

developed elsewhere in simplified contexts (Majda and Holen 1997; Grote and Majda 1997; DiBattista and Majda 1999, manuscript submitted to *Physica D*).

Acknowledgments. The authors thank John Marshall for his encouragement and helpful comments provided

through the course of this work. M. DiBattista is supported as a post-doctoral fellow at the Courant Institute by Grants NSF DMS-9625795 and ONR N00014-96-0043. The research of A. Majda is partially supported by Grants ONR N00014-96-0043, NSF DMS-9625795, and ARO DAAG55-98-1-0129.

REFERENCES

- Alverson, K., and W. Owens, 1996: Topographic preconditioning of open ocean deep convection. *J. Phys. Oceanogr.*, **26**, 2196–2213.
- Bretherton, F. B., and D. B. Haidvogel, 1976: Two-dimensional flow above topography. *J. Fluid Mech.*, **78**, 129–154.
- Carnevale, G. F., and J. S. Frederiksen, 1987: Nonlinear stability and statistical mechanics of flow over topography. *J. Fluid Mech.*, **175**, 157–181.
- Cummins, P. F., and G. Holloway, 1994: On eddy–topographic stress representation. *J. Phys. Oceanogr.*, **24**, 700–706.
- DiBattista, M. T., A. J. Majda, and B. Turkington, 1998: Prototype geophysical vortex structures via large-scale statistical theory. *Geophys. Astrophys. Fluid Dyn.*, **89**, 235–283.
- Grote, M. J., and A. J. Majda, 1997: Crude closure dynamics through large scale statistical theories. *Phys. Fluids*, **9**, 3431–3442.
- Hogg, N. G., 1973: The preconditioning phase of MEDOC 1969. II: Topographic effects. *Deep-Sea Res.*, **20**, 449–459.
- , and H. M. Stommel, 1985: Hetonic explosions: The breakup and spread of warm pools as explained by baroclinic point vortices. *J. Atmos. Sci.*, **42**, 1465–1476.
- Holloway, G., 1986: Eddies, waves, circulation, and mixing: Statistical geofluid mechanics. *Annu. Rev. Fluid Mech.*, **18**, 91–147.
- , 1992: Representing topographic stress for large-scale ocean models. *J. Phys. Oceanogr.*, **22**, 1033–1046.
- James, I. N., 1987: Suppression of baroclinic instability in horizontally sheared flows. *J. Atmos. Sci.*, **44**, 3710–3720.
- Jaynes, E. T., 1957: Information theory and statistical mechanics. *Phys. Rev.*, **106**, 620–630.
- Kazantsev, E., J. Sommeria, and J. Verron, 1998: Subgrid-scale eddy parameterization by statistical mechanics in a barotropic ocean model. *J. Phys. Oceanogr.*, **28**, 1017–1042.
- Kraichnan, R. H., 1975: Statistical dynamics of two-dimensional flow. *J. Fluid Mech.*, **67**, 155–175.
- Lamperti, J., 1966: *Probability Theory*. Benjamin, 150 pp.
- Legg, S., and J. Marshall, 1993: A heton model of the spreading phase of open-ocean deep convection. *J. Phys. Oceanogr.*, **23**, 1040–1056.
- , and —, 1998: The influence of the ambient flow on the spreading of convective water masses. *J. Mar. Res.*, **56**, 107–139.
- , H. Jones, and M. Visbeck, 1996: A heton perspective of baroclinic eddy transfer in localized ocean deep convection. *J. Phys. Oceanogr.*, **26**, 2251–2266.
- , J. McWilliams, and J. Gao, 1998: Localization of deep ocean convection by a geostrophic eddy. *J. Phys. Oceanogr.*, **28**, 944–970.
- Maded, G., F. Lott, P. Delecluse, and M. Crepon, 1996: Large-scale preconditioning of deep-water formations in the northwestern Mediterranean Sea. *J. Phys. Oceanogr.*, **26**, 1393–1408.
- Majda, A. J., and M. Holen, 1997: Dissipation, topography, and statistical theories for large-scale coherent structure. *Comm. Pure Appl. Math.*, **50**, 1183–1234.
- Marshall, J., and F. Schott, 1999: Open-ocean convection: Observations, theory and models. *Rev. Geophys.*, **37**, 1–64.
- Miller, J., P. B. Weichman, and M. C. Cross, 1992: Statistical mechanics, Euler's equation, and Jupiter's Red Spot. *Phys. Rev. A*, **45**, 2328–2359.
- Mu, M., Q. Zeng, T. G. Shepherd, and L. Yongming, 1994: Nonlinear stability of multilayer quasi-geostrophic flow. *J. Fluid Mech.*, **264**, 165–184.
- Nakamura, N., 1993: An illustrative model of instabilities in meridionally and vertically sheared flows. *J. Atmos. Sci.*, **50**, 357–375.
- Pedlosky, J., 1979: *Geophysical Fluid Dynamics*. Springer, 624 pp.
- Robert, R., 1991: A maximum entropy principle for two-dimensional Euler equations. *J. Stat. Phys.*, **65**, 531–553.
- Salmon, R., G. Holloway, and M. C. Hendershott, 1976: The equilibrium statistical mechanics of simple quasi-geostrophic models. *J. Fluid Mech.*, **75**, 691–703.
- Turkington, B., 1999: Statistical equilibrium structures and coherent states in two-dimensional turbulence. *Comm. Pure Appl. Math.*, **52**, 781–810.
- , and N. Whitaker, 1996: Statistical equilibrium computations of coherent structures in turbulent shear layers. *SIAM J. Sci. Comput.*, **17**, 1414–1433.